

Journal of Geophysical Research: Solid Earth

RESEARCH ARTICLE

10.1002/2015JB011982

Key Points:

- Wave gradiometry is applied to USArray in the eastern United States
- Wave gradiometry parameters provide useful constraints for 3-D modeling
- Two Rayleigh wave low-velocity zones are observed along Appalachian chain

Correspondence to:

Y. Liu,
yuanyuan.liu@stonybrook.edu

Citation:

Liu, Y., and W. E. Holt (2015), Wave gradiometry and its link with Helmholtz equation solutions applied to USArray in the eastern U.S., *J. Geophys. Res. Solid Earth*, 120, 5717–5746, doi:10.1002/2015JB011982.

Received 24 FEB 2015

Accepted 20 JUL 2015

Accepted article online 31 JUL 2015

Published online 27 AUG 2015

Wave gradiometry and its link with Helmholtz equation solutions applied to USArray in the eastern U.S.

Yuanyuan Liu¹ and William E. Holt¹¹Department of Geosciences, Stony Brook University, Stony Brook, New York, USA

Abstract Wave gradiometry is an array processing technique utilizing the shape of seismic wavefields captured by USArray TA stations to determine fundamental wave propagation characteristics. We first explore a compatibility relation that links the displacement spatial gradients to seismogram displacements and velocities through two unknown coefficients, \vec{A} and \vec{B} . These coefficients are solved for through iterative, damped least squares inversion to provide estimates of phase velocity, back azimuth, radiation pattern, and geometrical spreading. We show that the \vec{A} coefficient corresponds to the gradient of logarithmic amplitude, and the \vec{B} coefficient corresponds approximately to the local wave slowness. \vec{A} and \vec{B} vector fields are interpolated to explore a second compatibility relation through solutions to the Helmholtz equation. For most wavefields passing through the eastern U.S., we show that the \vec{A} coefficients are generally orthogonal to the \vec{B} coefficients. Where they are not completely orthogonal, there is a strong positive correlation between $\nabla \cdot \vec{B}$ and changes in geometrical spreading, which can be further linked with areas of strong energy focusing and defocusing. We finally obtain isotropic Rayleigh wave phase velocity maps for 15 periods between 20 and 150 s, by stacking results from 37 earthquakes, which show a velocity change along the approximate boundary of the early Paleozoic continental margin. We also observe two low-velocity anomalies, one centered over the central Appalachians where Eocene basaltic volcanism has occurred and the other within the northeastern U.S., possibly associated with the Great Meteor Hotspot track.

1. Introduction

Embedded within the North American continental lithosphere is the history of continental growth, with many ancient terranes that have accreted since the Archean, including the Superior, Wyoming, Yavapai, and Mazatzal Provinces, along with major structures associated with the Grenville and Appalachian orogenies [Whitmeyer, 2007]. Furthermore, the continental interior contains several ancient rift structures [Liang and Langston, 2008]. Studies coming out of USArray have already revealed many exciting details about the crust and upper mantle beneath western and central North America [Brudzinski and Allen, 2007; Lin et al., 2008; Sigloch et al., 2008; Yang and Ritzwoller, 2008; West et al., 2009; Cao and Levander, 2010; Schmandt and Humphreys, 2010; Yuan and Romanowicz, 2010; Levander et al., 2011; Obrebski et al., 2011; Schmandt and Humphreys, 2011; Shen et al., 2013a, 2013b; Evanzia et al., 2014; Langston and Horton, 2014; Pollitz and Mooney, 2014; Porritt et al., 2014]. The lithosphere within these regions shows major lateral heterogeneity, with a complex upper mantle structure profoundly influenced by the history of subduction. Details for the eastern U.S., however, are only now beginning to emerge [Burdick et al., 2014; Lin et al., 2014; Schmandt and Lin, 2014; Jin and Gaherty, 2015]. One major question identified within the EarthScope Science Plan is whether seismic studies can reveal if these major terrane boundaries, and province interiors, have a crust/mantle signature [Williams et al., 2010]. Second, what can the resolved structures tell us about continental accretion processes? Does the central and eastern U.S. lithosphere show similar heterogeneity as the western U.S.? Resolving lithosphere heterogeneity not only has implications for improving our understanding about the evolution of the continent, it also provides information that improves our understanding of the present-day dynamics of the North American lithosphere. That is, resolving structure provides constraints for temperature and possibly composition, which in turn provides constraints for density, internal body forces, and rheological heterogeneity. This information feeds into dynamic models [e.g., Ghosh and Holt, 2012; Ghosh et al., 2013] of intraplate stress and strain, necessary for understanding intraplate earthquakes, an important goal of EarthScope [Liang and Langston, 2008; Williams et al., 2010].

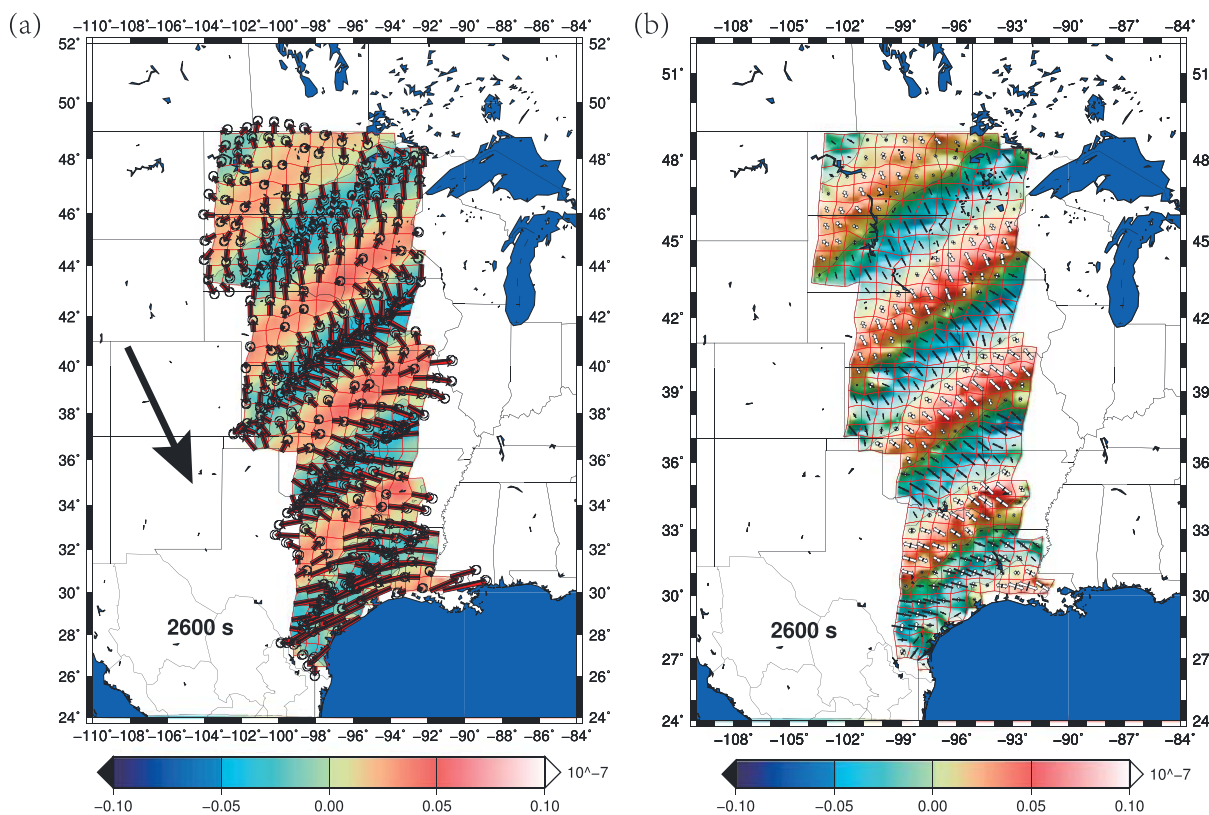


Figure 1. (a) Snapshot of the horizontal wavefields propagating through USArray TA Stations at 2600 s after the original time, from 11 March 2011 Great Tohoku-Oki earthquake. Red vector is observed horizontal displacement (with 95% confidence error ellipse), and the black vector is the model field predicted by the bicubic spline interpolation (described later). The contours show the spatial gradients of displacement field. The black arrow indicates the approximate wave propagation direction. (b) Contoured dilatational component of the strain field (spatial gradients) associated with Rayleigh wave. Principal axes of horizontal strain are also shown (bold = compressional; open = extensional).

Most traditional techniques in seismology, such as traveltimes tomography, receiver function, and shear wave splitting, apply some averaging methods, which treat each seismic station as an isolated observation [Liang and Langston, 2009]. This may smooth out or ignore wavefield amplitude differences that reflect real structure or complexity. The wave gradiometry method, however, is designed to take advantage of the spatial variations of wave amplitudes sampled by the dense array and resolve structure and propagation effects that cannot be derived strictly from the averaging methods [Langston, 2007a].

We now have an important opportunity to apply the wave gradiometry technique to the wavefields sampled by dense USArray Transportable Array (TA) stations (Figure 1). This observational approach, involving quantification of the shape of wavefield, is the next important step in seismology that, when combined with theory, has the potential to lead to new important discoveries regarding structural complexity and wavefield propagation characteristics. This work involves further development and use of wave gradiometry. We have implemented several new adaptations, including treatment of continuous displacement gradient fields within subarrays and a solution method for the Helmholtz equation. We show that gradiometry parameters can be used to investigate an approximation to the Helmholtz equation solution [Wielandt, 1993], as well as providing insight into the transport equation [Cerveny, 2005]. The gradiometry method is applied to multiple events recorded by USArray and reveals a rich field of information for each event, including significant effects of focusing and defocusing of energy, along with associated variations in geometrical spreading, radiation pattern, and back azimuth.

Gradiometry results for 55 s Rayleigh waves are described for four events. We also provide isotropic phase velocity maps in the eastern U.S. for 15 periods, by stacking results from 37 earthquakes. However, a detailed and comprehensive analysis of how spatial variations of gradiometry parameters are linked with 3-D structure modeling, including azimuthal anisotropy effects, is reserved for future analysis.

2. Methodology

In a Cartesian coordinate system, the solution to the wave equation can be written as

$$u(t, x, y) = G(x, y)f(t - p_x(x - x_0) - p_y(y - y_0)) \quad (1)$$

where u represents the displacement field, G represents the wave amplitude variation across space, f represents the phase variation as a function of time, t , and location $(x - x_0, y - y_0)$, p_x and p_y are components of the horizontal slowness in the x and y directions, respectively. Though equation (1) is a compatibility relation for a single dominant phase, we refer to the fact that *Langston* [2007a] showed that simultaneously arriving waves with the same frequency content generally do not provide a problem with the gradiometry treatment/approximation, so long as the amplitude of one of the two arrivals is small (at the noise level). Differentiating equation (1) gives us a set of equations, which link the spatial gradients to important wavefield propagation parameters [*Langston*, 2006, 2007a, 2007b, 2007c; *Liang and Langston*, 2009]

$$\frac{\partial u}{\partial x} = A_x \cdot u + B_x \cdot \frac{\partial u}{\partial t} \quad (2)$$

$$\frac{\partial u}{\partial y} = A_y \cdot u + B_y \cdot \frac{\partial u}{\partial t} \quad (3)$$

where

$$A_x = \frac{\partial G(x, y)}{\partial x} \cdot \frac{1}{G(x, y)} \quad A_y = \frac{\partial G(x, y)}{\partial y} \cdot \frac{1}{G(x, y)} \quad (4)$$

$$B_x = - \left[p_x + \frac{\partial p_x}{\partial x} (x - x_0) \right] \quad B_y = - \left[p_y + \frac{\partial p_y}{\partial y} (y - y_0) \right] \quad (5)$$

Integrating B_x and B_y over the interval $[x_0, x]$ gives the slowness in the x and y directions

$$p_x = -\frac{1}{x - x_0} \int_{x_0}^x B_x dx \quad p_y = -\frac{1}{y - y_0} \int_{y_0}^y B_y dy \quad (6)$$

When $x \rightarrow x_0$ and $y \rightarrow y_0$, the limit of equation (6) can be solved as

$$p_x(x_0) = -B_x(x_0) \quad p_y(y_0) = -B_y(y_0) \quad (7)$$

In general, the displacements, the spatial gradients, and the time derivatives (velocity) of displacement field, measured at a single seismic station, can be used through equations (2) and (3) to iteratively solve for the \vec{A} and \vec{B} coefficients (discussed later in section 2.2). Then the following relations may be used through equations (4) and (7) to find phase velocity v , back-azimuth θ , radiation pattern $A_\theta(\theta)$, and geometrical spreading $A_r(\theta)$ [*Liang and Langston*, 2009]

$$v = \left(B_x^2 + B_y^2 \right)^{-\frac{1}{2}} \quad (8)$$

$$\theta = \tan^{-1} \left(\frac{B_x}{B_y} \right) \quad (9)$$

$$A_\theta(\theta) = \frac{\partial G}{\partial \theta} \frac{1}{G} = r(A_x \cos \theta - A_y \sin \theta) \quad (10)$$

$$A_r(\theta) = \frac{\partial G}{\partial r} \frac{1}{G} = A_x \sin \theta + A_y \cos \theta \quad (11)$$

where r is the epicentral distance for the master station. There is a sign difference for $A_r(\theta)$ between equation (11) and equation (7) in *Liang and Langston* [2009]. We believe that the sign in *Liang and Langston* [2009] is a typo, as the correct expression is given by equation (10) in *Langston* [2007b].

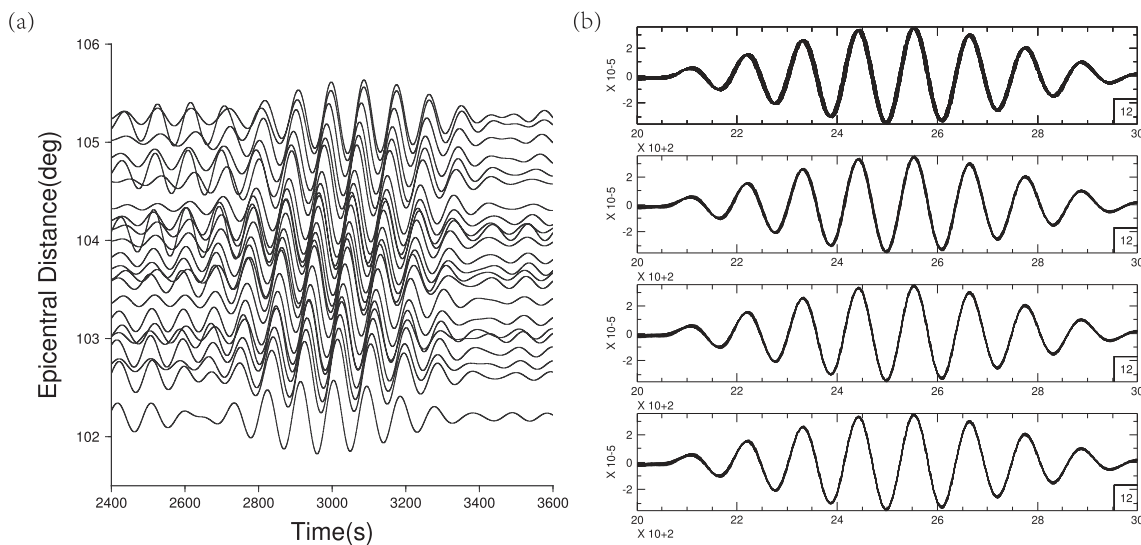


Figure 2. (a) Bandpass filtered waveforms recorded by USAArray TA station D28A and its supporting stations from 23 October 2011, earthquake near Turkey. The dominant phase is Rayleigh wave. (b) Stack of shifted waveforms for the subarray in Figure 2a, after applying reducing velocity method followed by least squares inversion for slowness perturbation. In Figure 2b the fourth row shows the final alignment after four iterations. The similarities are significant, but it is the spatial amplitude variations that carry wavefield characteristics along with the structural information across the space [Liang and Langston, 2009].

Liang and Langston [2009] applied wave gradiometry to USAArray data in the western U.S. They assumed that the wavefield parameters are constant across a given subarray, which is of order 200–400 km in dimension. In our work, we assume that the spatial gradients, and associated wave parameters, within a subarray define a spatially variable and continuous field. Being spatially continuous, we solve for the local values of wave parameters at each master station (x_0, y_0) , and thus, B_x and B_y represent the local wave slowness at position (x_0, y_0) . It is thus important to have a station spacing capable of resolving spatial gradients in the vicinity of the master station. We will show later that the station spacing in USAArray configuration is capable of resolving significant wavefront curvature for periods longer than 20 s, caused by focusing and defocusing of energy.

2.1. Reducing Velocity Method

The supporting stations are found within 200 km radius of the master station, which is less than three wavelengths of the shortest period (20 s) to prevent the phase delay between two stations from exceeding the period of observation [Jin and Gaherty, 2015]. The reducing velocity method, as introduced by Langston [2007b], is applied to each subarray, which may effectively decrease the phase move-out and spatial gradients variations between the master station and its supporting stations [Liang and Langston, 2009].

The waveforms of supporting stations within a subarray are shifted relative to the master station, based on the distance and the mean velocity between the master station and its supporting stations. After applying the time shift, any spatial gradients of the displacement field in equations (2) and (3) are associated with normalized gradients of amplitude (\vec{A} coefficients) and perturbations to the slowness estimate (\vec{B} coefficients) [Liang and Langston, 2009]. Initially, we assume a uniform phase velocity across the subarray (3.8 km/s for periods shorter than 50 s and 4.0 km/s for periods longer than 60 s). The perturbation in slowness is estimated to define a new reducing velocity. With updated velocity estimates at all stations, the wavefields are shifted again, followed by new estimates of the spatial gradients and then new least squares inversion for the coefficients. This process is repeated until convergence is achieved (usually four iterations, Figure 2).

2.2. Determining Spatial Gradient Tensor Field

Wave gradiometry equations (2) and (3) requires estimation of the spatial gradients of displacement wavefield. We interpolate the displacement field to return continuous estimates of the gradient tensor field within the subarray. The technique is a modification of methods used to analyze GPS data [e.g., Holt *et al.*, 2000a, 2000b; Beavan and Haines, 2001; Holt and Shcherbenko, 2013]. The displacement gradient tensor field is determined on a regular grid, with grid area spacing of $0.25^\circ \times 0.25^\circ$. Regularization of the solution on this grid consists of obtaining the sharpest estimate of displacement gradient tensor field possible that can be supported by

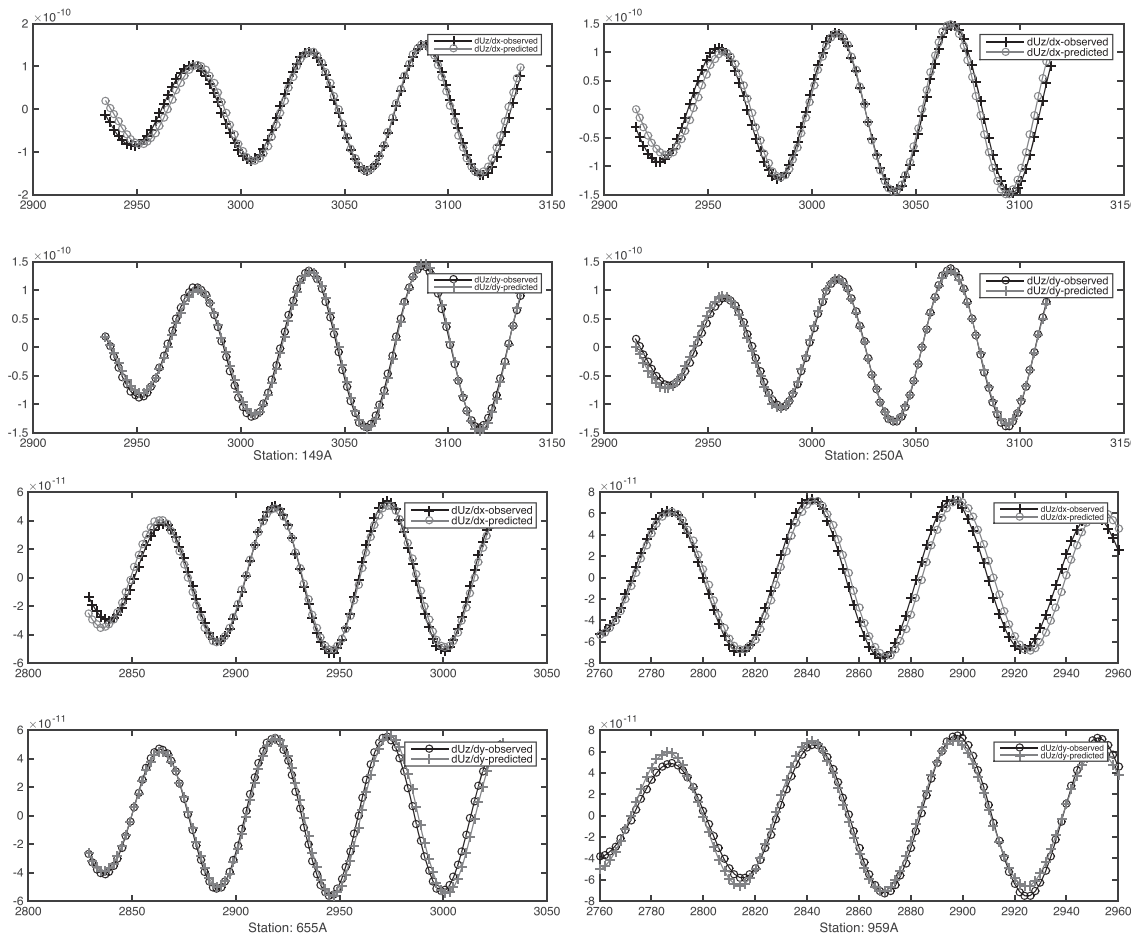


Figure 3. Observed spatial gradients of displacement field (black crosses) obtained from bicubic spline interpolation and the predicted spatial gradients (grey circles) using resolved \vec{A} and \vec{B} coefficients in equations (2) and (3), for 55 s Rayleigh wave recorded at TA stations: 149A, 250A, 655A, and 959A.

the displacement data (shifted wavefields within the subarray). The smoothing of the solution is controlled through optimization of the following functional in a formal least squares inversion of the displacement field

$$\chi = \sum_{\text{cells}} \sum_{ijkl} (\hat{e}_{ij})^T V_{ijkl}^{-1} (\hat{e}_{kl}) + \sum_{\text{knots}} \sum_{ij} (\hat{u}_i - u_i^{\text{obs}})^T V_{ij}^{-1} (\hat{u}_j - u_j^{\text{obs}}) \quad (12)$$

where V_{ijkl} is a weighting matrix for model strains, V_{ij} is the variance-covariance of displacement field, \hat{e}_{ij} is the model strain, and \hat{u}_i and u_i^{obs} are the predicted and observed displacements at a given time, respectively. The fitting algorithm that minimizes equation (12) is equivalent to a finite element method that satisfies force balance equations (spherical earth). The solution provides a best fit (in least squares sense) to the displacement field, while the model second invariant of the strain tensor field is minimized. The methodology solves the weak formulation of the linear problem, where the basis functions for the displacements are higher order elements involving the Bessel form of bicubic spline interpolation on a generally curvilinear grid of quadrilateral subdomains ($0.25^\circ \times 0.25^\circ$ grid) [De Boor, 1987; Beavan and Haines, 2001]. The final model predicts a continuous displacement gradient tensor field, with a posteriori model variance-covariance matrices [Haines and Holt, 1993; Beavan and Haines, 2001] for $\frac{\partial u}{\partial x}$ and $\frac{\partial u}{\partial y}$, which can be used to determine wave gradiometry parameter uncertainties [Aster et al., 2011]. Finer grid spacing can be adapted to problems supported by dense station spacing. Furthermore, we have tested different grid spacings for the USArray TA stations configuration and found that this chosen spacing is adequate for providing a good match to the time series, along with stable displacement gradient estimates. For each event we analyzed, there are around 600–800 time series of straingrams (two for each station) that are used to provide full gradiometry parameter estimates for the region covered. Figure 3 shows the typical match of the predicted and observed straingrams, where the predicted straingrams are determined using gradiometry coefficients (discussed in section 2.3 below).

The weighting matrix $V_{ij,kl}$ has an influence on the smoothing of model parameter estimates for interpolated displacements and inferred model displacement gradients. The weighting matrix is isotropic, which involves the assumption that the elastic medium has a linear relation between stress and strain. The diagonal elements, controlled by a single adjustable parameter, have an influence on how close the displacement field is fit by the model. It is important not to overfit the displacements, which can cause strain artifacts in the presence of significant noise. Thus, the size of the isotropic value is adjusted until a reduced chi-square misfit between predicted and observed displacements reaches 1. This reduced chi-square misfit depends on the size of the uncertainties in the displacement seismograms, which are unknown. After experimenting with a range of 0.1%–10% of the maximum magnitude of displacement field for the displacement uncertainties, we assume that the displacements have an uncertainty of 0.5%. Higher assumed uncertainty in displacement yields a smoother solution. We have found with benchmarking tests (discussed in section 2.6) that we are able to best resolve phase velocity variations if we obtain a close match to displacement fields in the USAArray data and that a choice of 0.5% works best for this. Such a low assumed error in displacement reflects the high quality of USAArray data [Liang and Langston, 2009; Lin et al., 2014; Porritt et al., 2014].

2.3. Solving for \vec{A} and \vec{B} -Coefficients

Note that \vec{A} and \vec{B} coefficients define a continuous field, just as the spatial gradients of displacement field define a continuous field. From equations (2) and (3), we first set up the inversion problem in the time domain

$$\mathbf{G}\mathbf{m} = \mathbf{d} \quad (13)$$

where \mathbf{G} is the matrix for displacements and the time derivatives of the displacement fields, \mathbf{m} contains the model coefficients \vec{A} and \vec{B} that we wish to solve for, and \mathbf{d} contains the spatial gradients of displacement fields. The typical analysis time window is 200 s, and the sampling is 2 s. Thus, the following system of equations can be applied to solve for A_x , A_y , B_x , and B_y at each seismic station, using an iterative, damped least squares inversion.

$$\begin{bmatrix} u|_{t_1} & \frac{\partial u}{\partial t}|_{t_1} \\ \vdots & \vdots \\ u|_{t_{101}} & \frac{\partial u}{\partial t}|_{t_{101}} \end{bmatrix} \times \begin{bmatrix} A_x \\ B_x \end{bmatrix} = \begin{bmatrix} \frac{\partial u}{\partial x}|_{t_1} \\ \vdots \\ \frac{\partial u}{\partial x}|_{t_{101}} \end{bmatrix} \begin{bmatrix} u|_{t_1} & \frac{\partial u}{\partial t}|_{t_1} \\ \vdots & \vdots \\ u|_{t_{101}} & \frac{\partial u}{\partial t}|_{t_{101}} \end{bmatrix} \times \begin{bmatrix} A_y \\ B_y \end{bmatrix} = \begin{bmatrix} \frac{\partial u}{\partial y}|_{t_1} \\ \vdots \\ \frac{\partial u}{\partial y}|_{t_{101}} \end{bmatrix} \quad (14)$$

Examination of the fit to hundreds of straingrams like those in Figure 3 suggests that the assumptions in the first compatibility relation in equations (2) and (3) are effective in matching the spatial gradients of the wavefield for each master station.

Singular value decomposition shows that the model eigenvector associated with the largest singular value points entirely in the \vec{A} coefficient direction. The other model eigenvector points entirely in the \vec{B} coefficient direction, and its singular value is generally 15 times smaller than the one associated with the \vec{A} coefficients. Therefore, in general, the slowness (\vec{B} coefficients) will be more sensitive to errors in the spatial gradients. We have found that the variances for spatial gradients are close to constant for any given time step. Thus, we assume that the data covariance: $\text{cov}[\mathbf{d}] = \sigma^2 \cdot \mathbf{I}$, where σ^2 is the formal estimate for the variance of the spatial gradients and \mathbf{I} is the identity matrix. Then the following simplified equation is used to determine the model covariance matrix:

$$\text{cov}[\mathbf{m}] = \sigma^2 \cdot \mathbf{V}_p \cdot (\lambda^{-2}) \cdot \mathbf{V}_p^T \quad (15)$$

where \mathbf{V}_p is the matrix containing model eigenvectors and λ is a diagonal matrix containing the model eigenvalues.

2.4. Solving for Structural Parameters

The phase velocity determined in conventional ray-based surface wave tomographic techniques, like the beam forming [Birtill and Whiteway, 1965] and two-station methods [Knopoff et al., 1966; Meier et al., 2004], is actually the local velocity of an individual wavefield based on the assumption of one dominate phase. This dynamic phase velocity depends not only on the underlying medium but also on the local geometry of the wavefield [Wielandt, 1993; Friederich et al., 1995; Pollitz and Snoker, 2010]. Wielandt [1993] points out that the dynamic phase velocity cannot be directly attributed to the structure and cannot be used as an input for tomographic structure inversion. Neglecting this fact can systematically bias the structure interpretation [Yang and

Forsyth, 2006; *Lin et al.*, 2009; *Pollitz and Snoker*, 2010]. The phase velocity in the Helmholtz equation is defined as the structural phase velocity, which is independent of specific geometry of the wavefield or source properties [Wielandt, 1993; Friederich et al., 1995; *Lin and Ritzwoller*, 2011]. Numerous theoretical and numerical studies [Friederich et al., 2000; Bodin and Maupin, 2008; *Lin and Ritzwoller*, 2011; *Jin and Gaherty*, 2015] have shown that in most cases, the dynamic phase velocity can differ substantially from the structural phase velocity for a single event. *Wielandt* [1993] showed that the solutions to the Helmholtz equation yield a local relationship: the deviation of the structural phase velocity from dynamic phase velocity depends on the first and second derivatives of logarithmic amplitude. *Lin and Ritzwoller* [2011] and *Jin and Gaherty* [2015] both showed that surface wave tomography can be improved by using amplitude measurements to construct a geographically localized correction via the Helmholtz equation, which accounts for the finite frequency effects accurately, and this correction should at least be used at periods longer than 50 s for USAArray TA stations [*Lin and Ritzwoller*, 2011].

Lin et al. [2009] and *Lin and Ritzwoller* [2011] addressed the solutions to the 2-D eikonal equation and the Helmholtz equation, respectively,

$$\frac{1}{c'(x,y)^2} = |\nabla \tau(x,y)|^2 \quad (16)$$

$$\frac{1}{c(x,y)^2} = |\nabla \tau(x,y)|^2 - \frac{\nabla^2 G(x,y)}{G(x,y)\omega^2} \quad (17)$$

where τ is the phase traveltimes, G is the wave amplitude at location (x,y) , the same as defined in equation (1), and ω is the angular frequency. Note that the Helmholtz equation is a second compatibility relation that we investigate, where the first compatibility relation involves equations (1)–(3). The Helmholtz equation governs the propagation of most classical wavefields in homogeneous, isotropic media [Wielandt, 1993]. *Lin and Ritzwoller* [2011] referred to c' as the apparent velocity (or dynamic velocity) and c as the corrected velocity (or structural velocity). The difference between equations (16) and (17) is described by the Laplacian of the amplitude field normalized by the amplitude and square of the angular frequency. This amplitude Laplacian term [*Lin and Ritzwoller*, 2011] permits a correct structural interpretation of surface waves in laterally homogeneous parts of the medium [Wielandt, 1993].

Here we show that the gradiometry coefficients that we have solved for can be used to approximate solutions for the Helmholtz equation for structural phase velocity. From equation (4), we know that the \vec{A} coefficient corresponds to the gradient of logarithmic amplitude

$$\vec{A} = \nabla \ln G = \frac{\nabla G}{G} \quad (18)$$

thus,

$$\vec{A}^2 + \nabla \cdot \vec{A} = \left(\frac{\nabla G}{G}\right)^2 + \frac{\nabla^2 G \cdot G - (\nabla G)^2}{G^2} = \frac{\nabla^2 G}{G} \quad (19)$$

We have compared our phase velocity results with two separate results [*Lin and Ritzwoller*, 2011; *Jin and Gaherty*, 2015] that used the same data sets (2009 Kuril Islands earthquake and 2007 Easter Island earthquake) and found a remarkable correspondence (discussed in section 2.5). The phase velocities determined from wave gradiometry \vec{B} coefficients through equation (8) are almost identical to the dynamic phase velocities determined from the gradients of phase traveltimes used in the Helmholtz tomography [*Lin and Ritzwoller*, 2011]. Thus, we have determined empirically that the use of equations (2) and (3) (the first compatibility relation) provides very similar estimates of wave slowness to other studies that use gradient of phase traveltime methods [*Lin and Ritzwoller*, 2011] and multichannel cross-correlation methods [*Jin and Gaherty*, 2015]. In our investigation of the second compatibility relation in the Helmholtz equation solution (17), we make the assumption (based on this similarity with two other studies) that the \vec{B} coefficient can be approximated as the local gradient of phase traveltimes:

$$|\vec{B}| = |\vec{p}| \approx \left| \frac{1}{c'} \right| = |\nabla \vec{\tau}| \quad (20)$$

But to be clear, we always relate the \vec{B} coefficient to the local ray parameter as part of its original definition in equations (1), (2), (3), and (7). Furthermore, we have found a close match between $\nabla \cdot \vec{B}$ (obtained from the 2009

Kuril Islands event) and the focusing/defocusing correction term in *Lin et al.* [2012] (discussed in section 2.5). This further substantiates our assumption that $\nabla \cdot \vec{B}$ can be approximated as the Laplacian of phase traveltme

$$\nabla \cdot \vec{B} \approx \nabla^2 \tau \quad (21)$$

Combining equations (17), (19), and (20), the structural phase velocity is determined by subtracting the amplitude correction term [*Lin and Ritzwoller*, 2011], involving \vec{A} , $\nabla \cdot \vec{A}$, and ω , from the dynamic phase velocity

$$\frac{1}{c^2} \approx |\vec{B}|^2 - \frac{\vec{A}^2 + \nabla \cdot \vec{A}}{\omega^2} \quad (22)$$

In order to find $\nabla \cdot \vec{A}$, we interpolate the \vec{A} coefficient vector field using the bicubic splines [*Beavan and Haines*, 2001], which is the same method used to obtain spatial gradients from the displacement field. *Wielandt* [1993] argued that the amplitude correction term provides real constraints on the structural wavenumber. *Lin and Ritzwoller* [2011] make these corrections to their estimates of gradient of phase traveltme measurements, and *Jin and Gaherty* [2015] also makes similar corrections to their estimates of local phase velocity. We have found a close match between our corrections compared to theirs for the same data sets (discussed in sections 2.5). However, before applying equation (22) to our gradiometry parameters, we assume that the acoustic Helmholtz equation remains approximately valid for elastic surface waves when the structure is slightly or smoothly inhomogeneous compared to the heterogeneity of the wavefield [*Wielandt*, 1993]. This is also born out by our gradiometry parameter results (see results in section 3.0 and summary in section 3.5).

We then address the transport equation [Cerveny, 2005] from the imaginary part of the solution to the 2-D Helmholtz equation

$$2 \cdot \nabla \tau(x, y) \cdot \frac{\nabla G(x, y)}{G(x, y)} - \nabla^2 \tau(x, y) = 0 \quad (23)$$

Substituting equations (18), (20), and (21) into (23) gives us

$$2 \cdot \vec{B} \cdot \vec{A} - \nabla \cdot \vec{B} = 0 \quad (24)$$

The first and second terms in the above equation are defined as “apparent amplitude decay” and “focusing/defocusing correction term,” respectively [*Lin et al.*, 2012]. We observe generally positive correlations between these two terms (Figure 4), in accord with the relation in equation (24). Furthermore, *Lin et al.* [2012] have used these terms to constrain local amplification factors in the western U.S. regions, which can be used to constrain density variations.

An inspection of gradiometry parameters for 12 October 2013, earthquake near Crete, shows an interesting pattern in relation to regional amplitude variations. The \vec{A} coefficients in Figure 5a, obtained from least squares inversion of equations (2) and (3), show patterns that are in accord with spatial variations of amplitudes in Figure 5b, which makes sense because the \vec{A} coefficients represent the gradient of logarithmic amplitude. These vectors point toward amplitude highs and away from amplitude lows. Note that the \vec{A} coefficient vector fields in Figure 5a do not result from taking derivatives of the static maximum amplitudes plotted in Figure 5b. Instead, these estimates arise from inversion of spatial gradients of displacement field for all time steps at each individual station. The correlation described above, however, provides confirmation that our method for estimating the coefficients from the spatial derivatives of the wavefield is robust.

The Laplacian of logarithmic amplitude ($\nabla \cdot \vec{A}$, contoured in Figure 5a), is used in the approximate solution to the Helmholtz equation (22). The \vec{B} coefficients (vector field in Figure 5c) point opposite to the wave propagation direction ($\vec{B} = -\vec{p}$). Note that this vector field shows systematic bending in places, reflecting focusing and defocusing of energy. Furthermore, $\nabla \cdot \vec{B}$ (contoured in Figure 5c) can be further used in solutions to the Helmholtz equation for laterally varying media in both velocity and density (described below). We will show later that $\nabla \cdot \vec{B}$ have a strong correlation with changes in geometrical spreading. The amplitude correction term that depends on the \vec{A} coefficients and $\nabla \cdot \vec{A}$ in Figure 5a can result in a velocity difference between dynamic and structural phase velocity as high as 0.4 km/s (Figure 5d).

The blue areas in Figure 5a shows locations where the amplitudes have maximum relative values. In such areas, $\vec{A} = 0$ and $\nabla \cdot \vec{A} < 0$, and the amplitude correction term yields a structural phase velocity less than

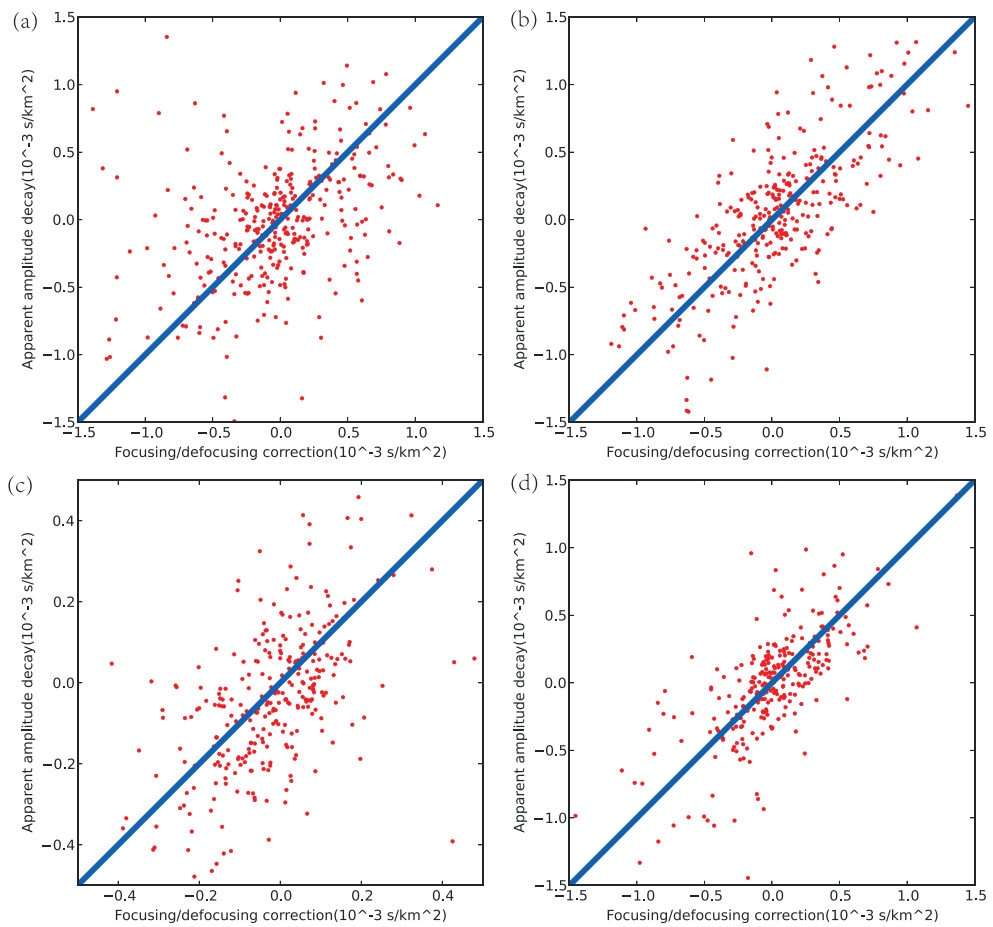


Figure 4. The correlation between the apparent amplitude decay ($2 \cdot \vec{A} \cdot \vec{B}$) and the focusing/defocusing correction term ($\nabla \cdot \vec{B}$) in the transport equation (24) for 55 s Rayleigh wave, where each red dot denotes the result at a station. The blue line is the best fitting straight line. (a) 25 October 2013, earthquake near Honshu ($M_w = 7.3$), (b) 2 February 2014, earthquake near Kermadec Island ($M_w = 6.6$), (c) 16 March 2014, earthquake near Chile ($M_w = 6.7$), and (d) 24 May 2014, earthquake in Aegean Sea ($M_w = 6.9$).

dynamic phase velocity (red areas in Figure 5d). In the red areas of Figure 5a, where the amplitudes have minimum relative values, we have $\vec{A} = 0$ and $\nabla \cdot \vec{A} > 0$, and the amplitude correction term yields a structural phase velocity greater than dynamic phase velocity (blue areas in Figure 5d) [Wielandt, 1993].

Figure 6 shows the probability density functions, mean value, and standard deviation for dynamic and structural phase velocity results at two TA stations. The distribution of structural phase velocities are generally more concentrated than the dynamic phase velocities, which may reflect the reduction of local wavefield geometry effects and random noise bias [Lin and Ritzwoller, 2011].

If both the phase velocity and the density are variable in a medium, the equivalent solutions to the Helmholtz equation for the acoustic case in such medium are

$$\frac{1}{c^2} = |\vec{B}|^2 - \frac{\vec{A}^2 + \nabla \cdot \vec{A} - \vec{A} \cdot \nabla(\ln \rho)}{\omega^2} \quad (25)$$

$$2 \cdot \vec{B} \cdot \vec{A} - \nabla \cdot \vec{B} = \vec{B} \cdot \nabla(\ln \rho) \quad (26)$$

This enables us to estimate the density by integrating in the direction of wave propagation [Wielandt, 1993]. Thus, in the future the gradiometry coefficients and the divergence of these coefficients (Figures 5a and 5c) can be used to obtain constraints on density variations when considering the acoustic case.

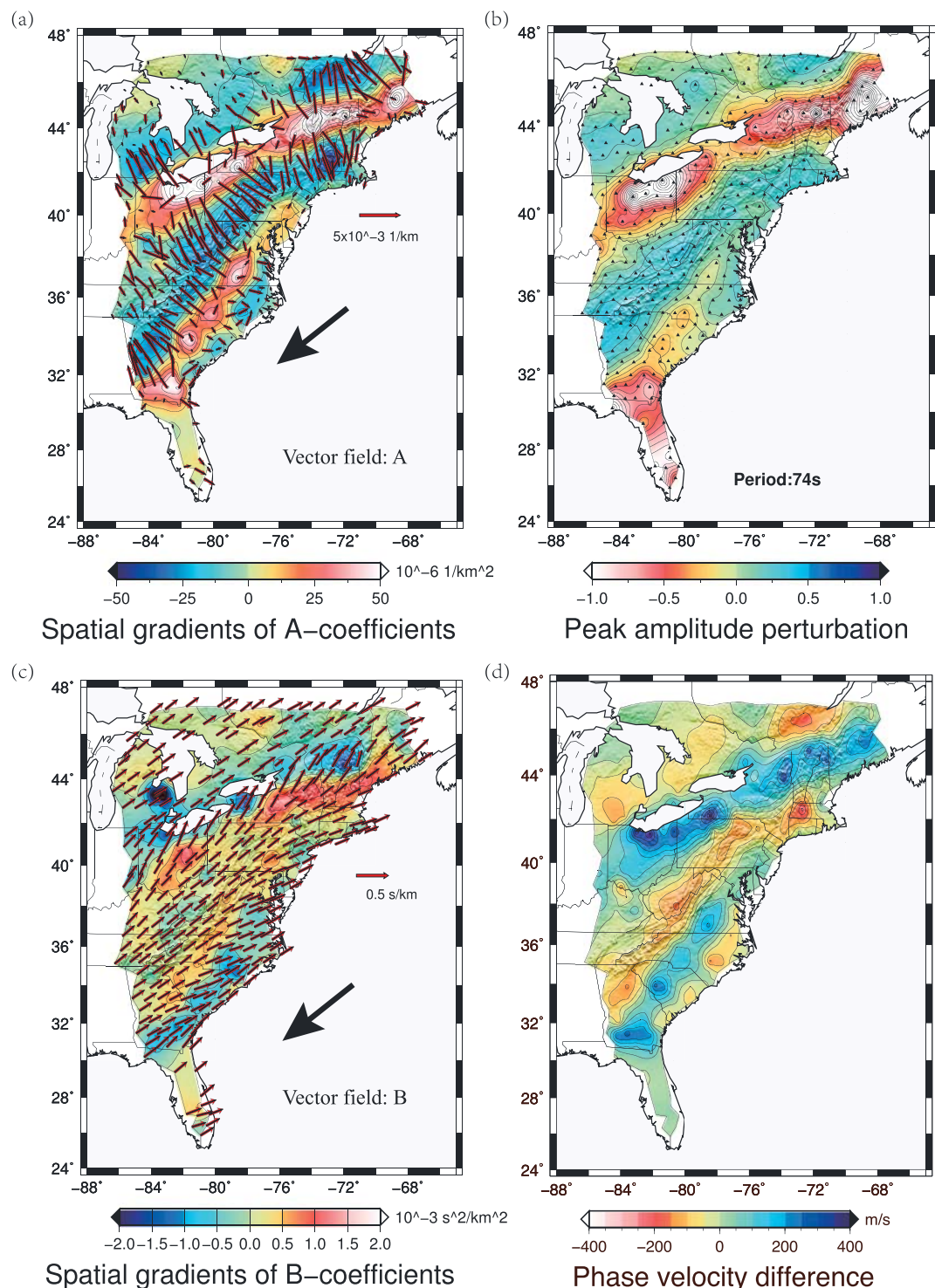


Figure 5. (a and c) The vectors represent the \vec{A} coefficients (gradients of logarithmic amplitude) and the \vec{B} coefficients field (horizontal slowness), respectively, for 74 s Rayleigh wave from 12 October 2013 earthquake near Crete. The contours correspond to $\nabla \cdot \vec{A}$ (Laplacian of logarithmic amplitude) and $\nabla \cdot \vec{B}$, which are separated by intervals of $25 \times 10^{-6} \text{ km}^{-2}$ and $0.5 \times 10^{-3} \text{ s}^2/\text{km}^2$, respectively. Note that the \vec{A} coefficient vectors generally point along steepest gradient toward amplitude highs and away from amplitude lows, and the \vec{B} coefficient vectors point opposite to wave propagation direction, which show systematic deflection of energy. The arrow indicates the approximate ray path. (b) The peak amplitude perturbation for Rayleigh wave phase. The stations are shown as triangles. (d) Dynamic and structural phase velocity differences calculated from amplitude correction terms in equation (22).

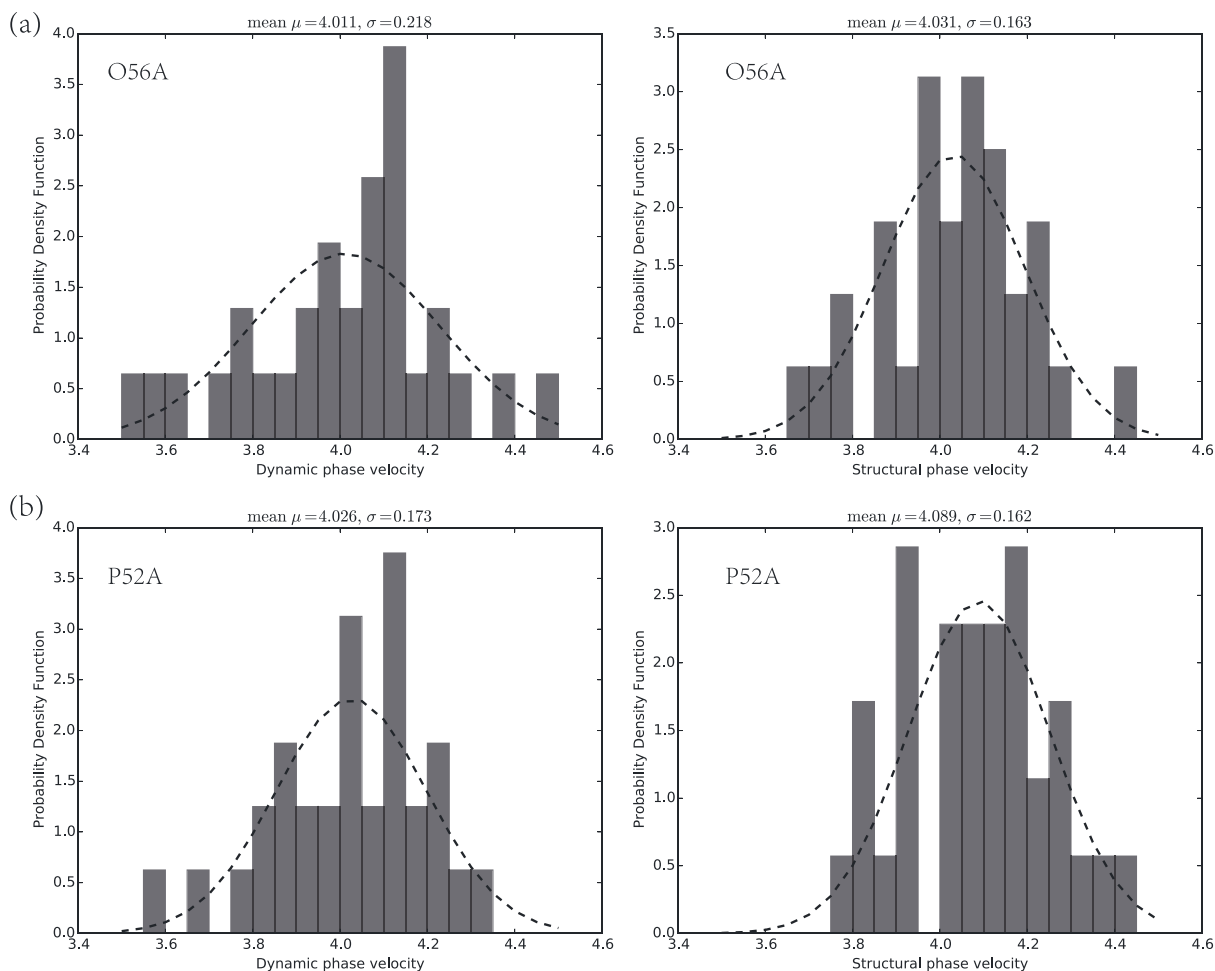


Figure 6. Percentage density function for 55 s Rayleigh wave dynamic and structural phase velocity at TA stations (a) O56A and (b) P52A. The mean velocity and standard deviation are also shown. The dashed lines indicate Gaussian fitting curves.

2.5. Benchmarking

We have experimented with two events: 7 April 2009, earthquake near Kuril Islands and 14 February 2007, earthquake near Easter Island, for 60 s Rayleigh wave. The close match between $\nabla \cdot \vec{B}$ (contoured in Figures 7a and 8a) and the focusing/defocusing maps in *Lin et al.* [2012] supports the approximate relation in equations (20) and (21). The patterns in amplitude Laplacian terms we obtain for both events (Figures 7b and 8b) are also quite similar to results from *Lin and Ritzwoller* [2011] and *Jin and Gaherty* [2015], and we thus share similar amplitude correction terms. Both the dynamic and structural phase velocity maps (Figures 7c and 7d and 8c and 8d) obtained using wave gradiometry parameters show very close consistencies with the results from *Lin and Ritzwoller* [2011] and *Jin and Gaherty* [2015] for the same data sets, which they obtain using different methods (Helmholtz tomography and multichannel cross-correlation method). Small differences (less than 10%) can be attributed to the possible differences in estimation of spatial derivatives of the amplitude field.

The least squares inversion requires a starting model. To find out how the starting velocity influences our final result, we have applied another two starting phase velocities (3.8 km/s and 4.2 km/s) to 60 s Rayleigh waves for Kuril Islands event. After four iterations, both the dynamic and structural velocity maps (Figure 9) are nearly identical to the ones starting with 4.0 km/s (Figures 7c and 7d). This confirms that the final solution for gradiometry parameters is not sensitive to the starting velocity guess.

For periods less than 40 s, there is a possibility of spatial aliasing of the wavefield because there are fewer than two stations covering the wavelength dimension. We have experimented with different starting velocities

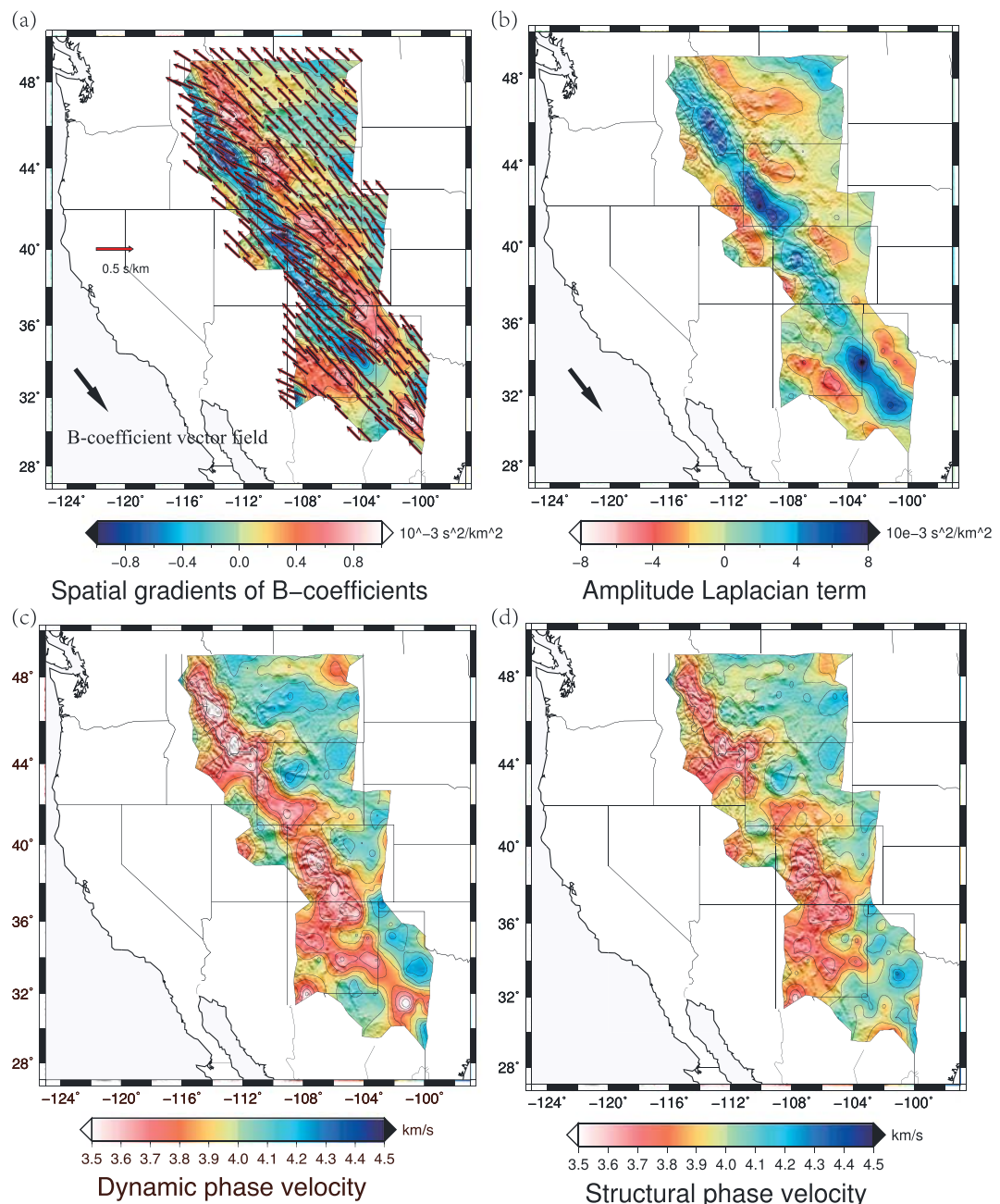


Figure 7. (a) \vec{B} coefficient vector fields, along with contoured $\nabla \cdot \vec{B}$ for 60 s Rayleigh wave from 7 April 2009 earthquake near Kuril Islands ($M_w = 6.8$). Contours are separated by intervals of $0.2 \times 10^{-3} \text{ s}^2/\text{km}^2$. (b) Amplitude Laplacian term in equation (17), calculated from \vec{A} coefficient field and its first derivative. Contours are separated by intervals of $2 \times 10^{-3} \text{ s}^2/\text{km}^2$. (c and d) Dynamic (apparent) and structural (corrected) phase velocity maps. Contours are separated by intervals of 0.1 km/s.

(3.4 km/s, 3.6 km/s and 3.8 km/s) for 20 s period Rayleigh waves and found only slight sensitivity for velocity results to starting model guess. However, for periods less than 40 s we do see that the gradients of logarithmic amplitude estimates (\vec{A} coefficients) are generally not as smooth as for longer period results, although similar trend distributions are still observed for these shorter periods (discussed in section 2.6). Spatial variations in amplitudes must be more than twice the station spacing (140 km) in order to be smoothly resolved. We will show later that our isotropic velocity results for short periods 20–40 s agree well with results from Jin and Gaherty [2015].

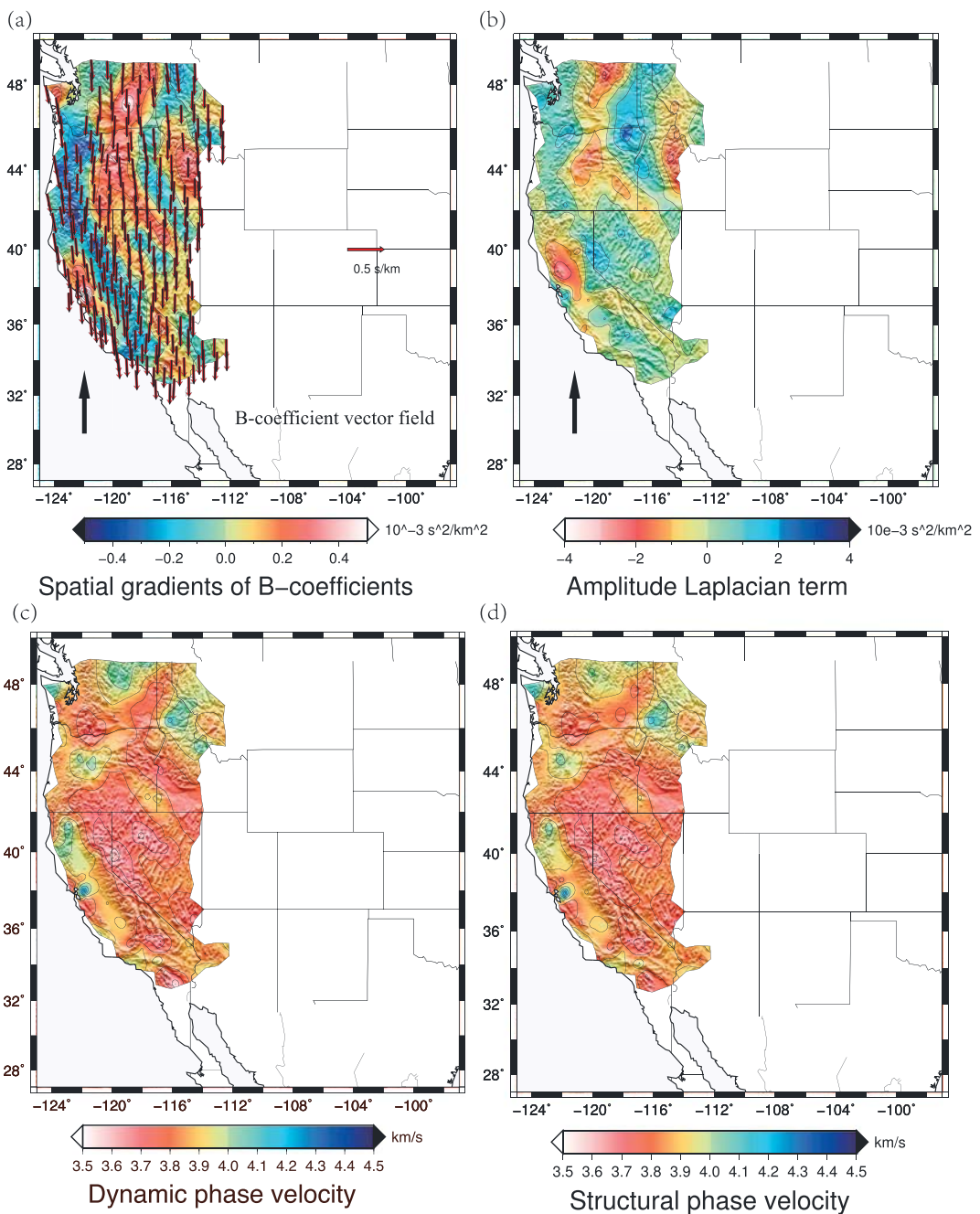


Figure 8. The same with Figure 7 but for the 14 February 2007 earthquake near Easter Island ($M_w = 5.7$).

2.6. Data Processing

We select teleseismic earthquakes with M_w larger than 6.0 and focal depth shallower than 50 km from Incorporated Research Institutes for Seismology (IRIS) Data Management Center. Earthquakes with significant-sized aftershocks that followed within less than 1 h of the main shock are not analyzed to avoid Rayleigh phase interferences. Only vertical component seismograms are analyzed, because they are not contaminated by Love wave or higher mode Rayleigh waves, and the noise levels are typically lower than horizontal components [Friederich *et al.*, 1995; Yang and Forsyth, 2006].

The broadband seismograms for each event are processed with the following procedures: (1) discard waveforms with the largest displacements more than two standard deviations beyond the mean values; (2) remove instrumental response, wave trends, and means; apply narrow bandpass filters to the displacement

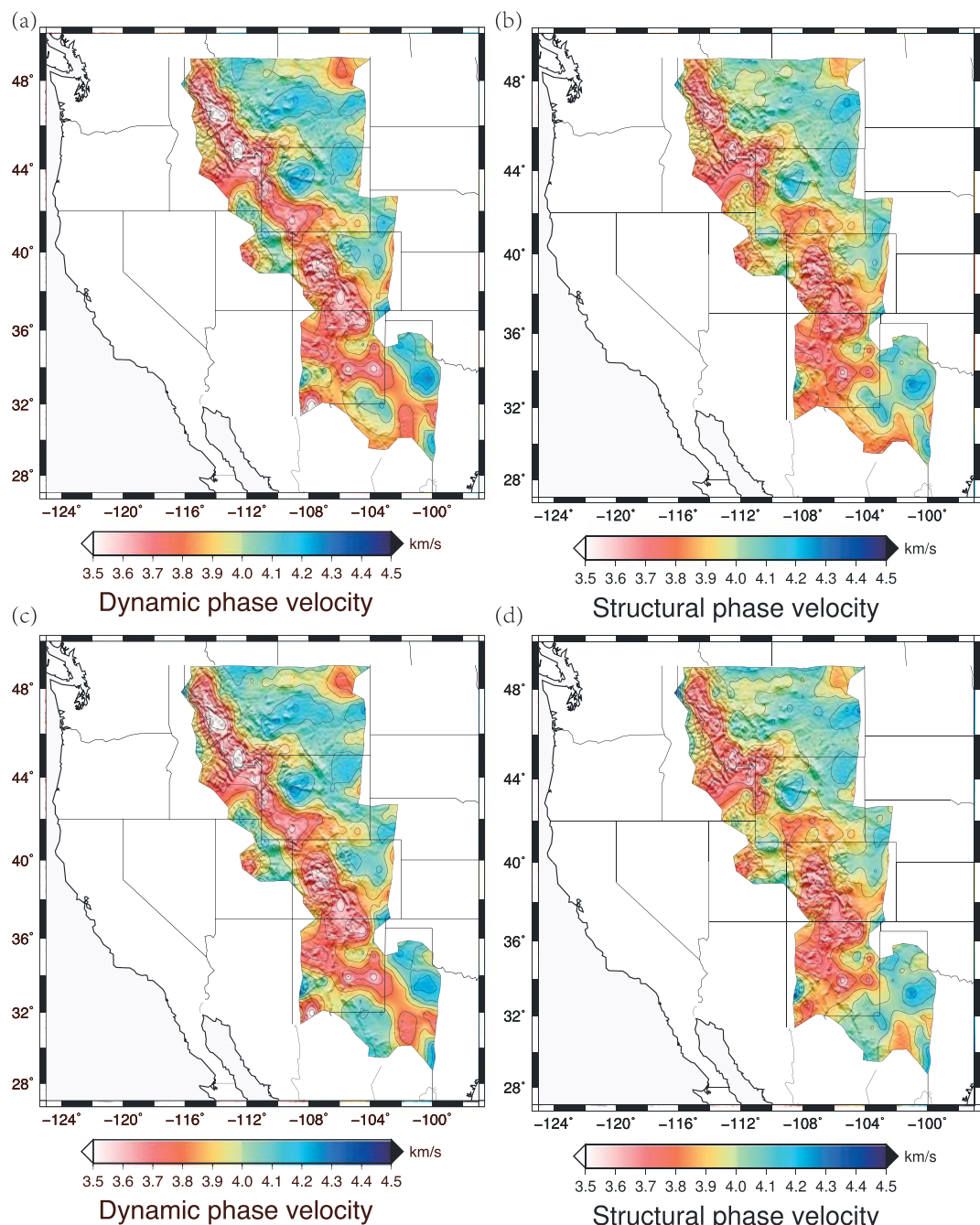


Figure 9. Dynamic and structural phase velocity maps for 60 s Rayleigh wave from earthquake near Kuril Islands, using (a and b) 3.8 km/s and (c and d) 4.2 km/s as starting phase velocity, respectively. Contours are separated by intervals of 0.1 km/s.

waveforms for 15 passbands with center periods ranging from 20 s to 150 s; (3) examine the waveforms and make sure the Rayleigh phase is clean and strong; (4) upload data to Extreme Science and Engineering Discovery Environment (XSEDE) parallel computing center [Towns *et al.*, 2014]; (5) generate 200 s time window for analysis based on Rayleigh phase arrival time; (6) remove subarrays with less than five supporting stations and apply reducing velocity method to shift waveforms within each subarray; (7) obtain the displacements, the spatial gradients, and the time derivatives of displacement field, (8) invert for \vec{A} and \vec{B} coefficients using least squares inversion; (9) use the iterated velocity as a new reducing velocity and repeat processes from steps (6) to (8) until the velocity differences between the two successive loops are smaller than 0.01 km/s

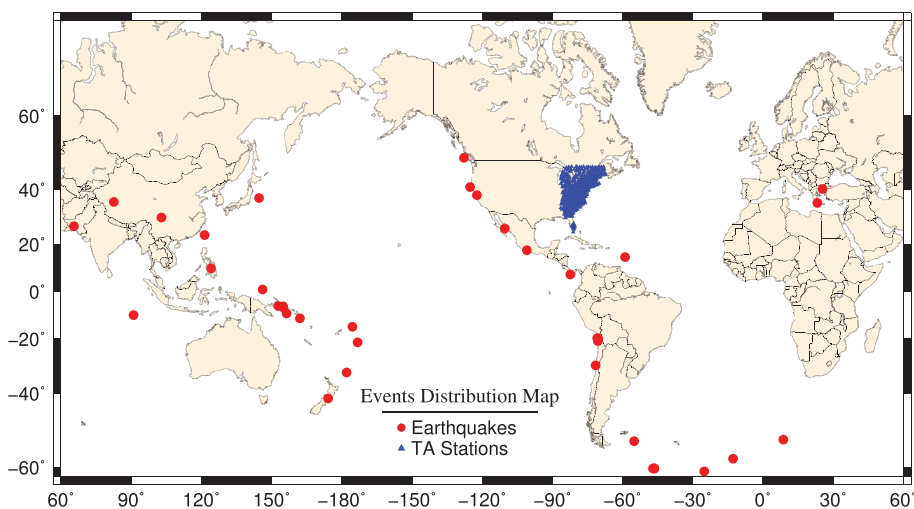


Figure 10. Earthquakes and USArray TA stations distribution map. The red dots mark the earthquake locations, and the blue triangles indicate the USArray TA Stations.

[Liang and Langston, 2009]; (10) interpolate the \vec{A} and \vec{B} coefficient fields to estimate the amplitude correction and focusing/defocusing terms, respectively; (11) calculate the structural phase velocity, back azimuth, radiation pattern, and geometrical spreading; (12) estimate structural phase velocity standard deviation from formal error estimates of spatial gradients of displacement field and \vec{B} coefficients [Aster et al., 2011]; and (13) stack structural phase velocity results from all events for isotropic phase velocity maps.

3. Gradiometry Results

Seismic records from 37 earthquakes are processed for around 450 USArray TA stations in the eastern U.S. (Figure 10, partial list in Table 1). The wave gradiometry method is only applied to Rayleigh waves here, but it can also be applied to Love waves, or even body waves [Liang and Langston, 2009; Sun and Helmberger, 2011; Jin and Gaherty, 2015].

The results of wave gradiometry parameters for four events are presented in Figures 11 and 12. Vector fields and contours in Figure 11 represent the \vec{A} coefficients (gradient of logarithmic amplitude) and $\nabla \cdot \vec{A}$ (Laplacian of logarithmic amplitude), respectively. The \vec{A} coefficients are associated with amplitude variations

Table 1. Partial List of Seismic Events Used in This Project

Time	Lat	Lon	Depth	Mag	Location	Stations
2013/04/20	30.31	102.89	14.0	6.6	Sichuan	346
2013/07/15	-60.86	-25.07	11.0	7.3	Sandwich	331
2013/09/24	26.97	65.52	15.0	7.7	Pakistan	357
2013/10/12	35.51	23.25	40.0	6.6	Crete	363
2013/10/25	-13.71	166.51	35.0	7.3	Honshu	353
2013/10/31	23.59	121.44	10.0	6.6	Taiwan	365
2013/11/16	-60.26	-47.06	9.9	6.8	Scotia	362
2013/11/17	-60.27	-46.40	10.0	7.7	Scotia	350
2013/11/25	-53.95	-55.00	11.8	7.0	Falkland	358
2014/02/02	-32.91	-177.88	44.3	6.6	Kermadec	328
2014/02/12	37.16	144.66	12.4	6.8	Xizang	369
2014/05/24	40.29	25.39	6.4	6.9	Aegean	370
2014/07/04	-6.23	152.81	20.0	6.5	Britain	267
2014/08/24	-122.31	38.22	11.3	6.0	Napa	234
2014/09/04	-173.26	-21.40	11.8	6.0	Tonga	246

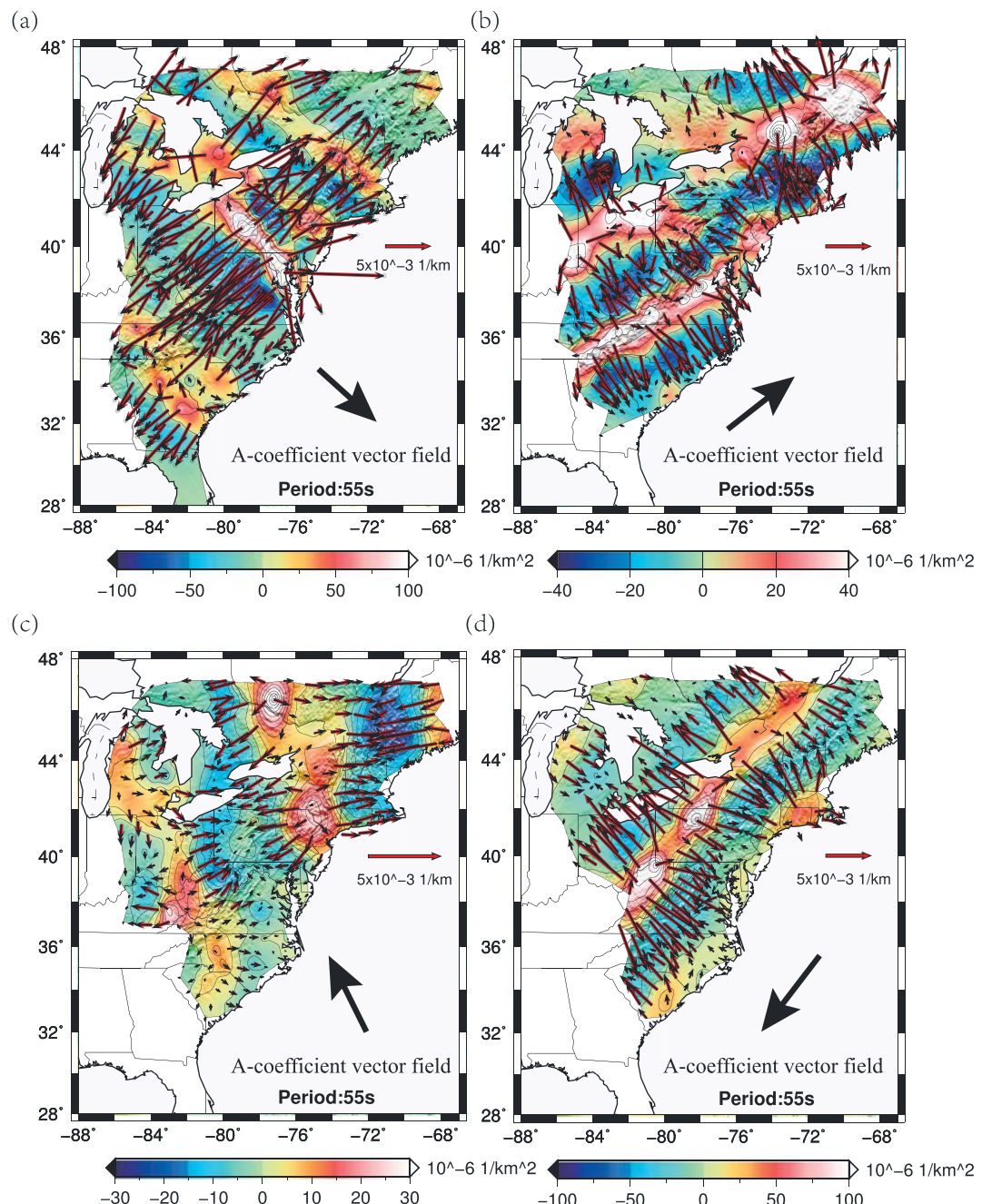


Figure 11. Vector fields are associated with \vec{A} coefficients and contours show $\nabla \cdot \vec{A}$ for 55 s Rayleigh wave from (a) 25 October 2013, earthquake near Honshu, (b) 2 February 2014, earthquake near Kermadec Island, (c) 16 March 2014, earthquake near Chile, and (d) 24 May 2014, earthquake in Aegean Sea. The large black arrows show approximate ray paths.

across space (geometrical spreading and radiation pattern), which can provide information related to focusing and defocusing of energy [Dahlen and Tromp, 1998; Liang and Langston, 2009]. The vector fields and contours in Figure 12 represent the \vec{B} coefficients (local wave slowness) and $\nabla \cdot \vec{B}$, respectively. From transport equation (24), when $\nabla \cdot \vec{B}$ is relatively small, \vec{A} and \vec{B} coefficient vectors must be orthogonal to each other [Wielandt, 1993]. We indeed find that the \vec{A} coefficients (Figure 11) are in general perpendicular to the \vec{B} coefficients (Figure 12), except in regions with large values of $\nabla \cdot \vec{B}$, where we argue that wavefields are either focusing or defocusing. \vec{A} coefficient vectors diverge (positive values of Laplacian of logarithmic amplitude) from regions of low relative amplitude and converge toward regions of higher relative amplitude (negative

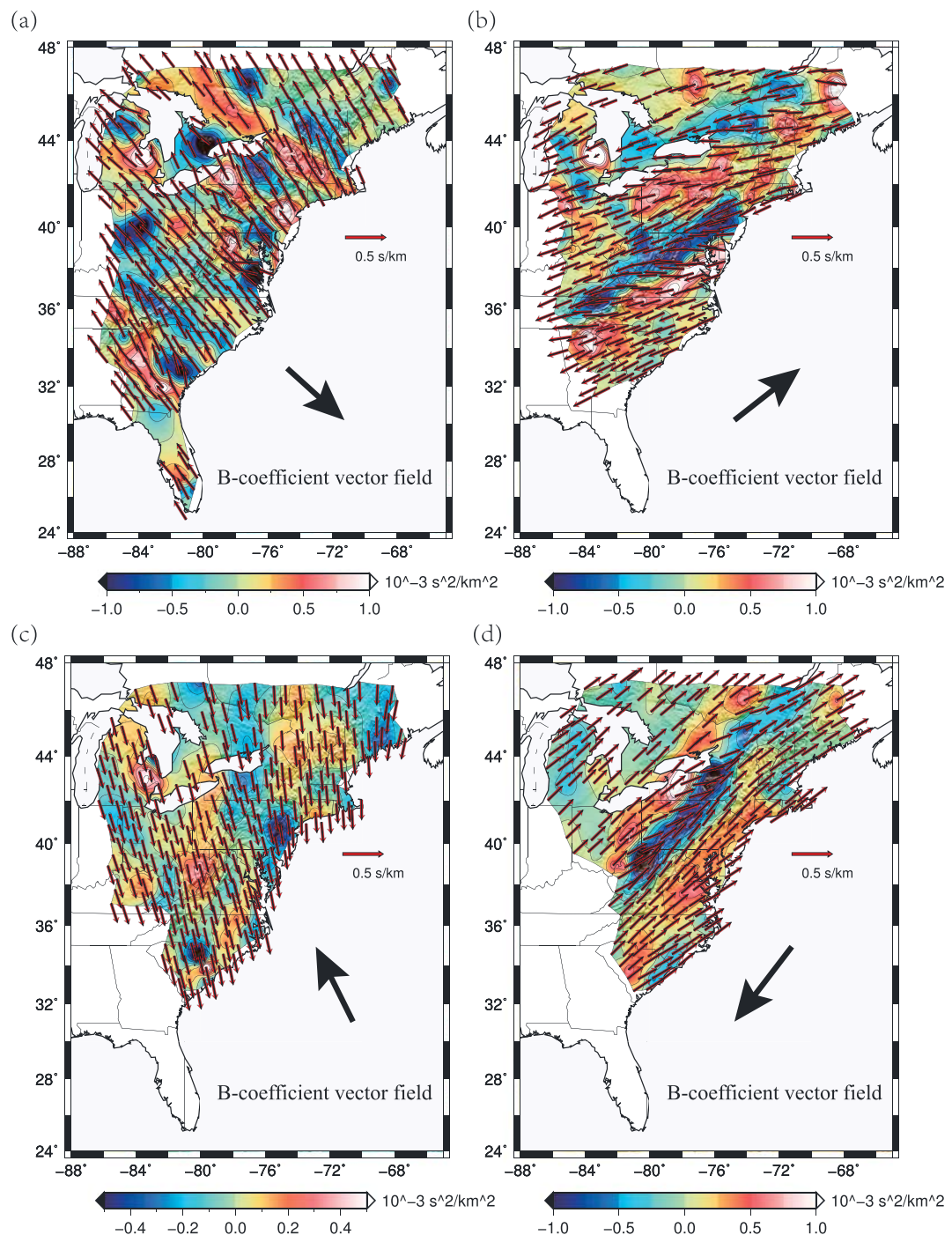


Figure 12. Vector fields are associated with \vec{B} coefficients and contours show $\nabla \cdot \vec{B}$ for 55 s Rayleigh wave from the same earthquakes in Figure 11.

values of Laplacian of logarithmic amplitude in Figure 11). The large variations of the \vec{A} and $\nabla \cdot \vec{A}$ are attributed to high amplitude change across space, since they involve the derivatives of logarithmic amplitudes.

We also show the \vec{A} and \vec{B} coefficient fields for 20 s Rayleigh waves obtained from two events we analyzed earlier (Figure 13). Both vector fields show characteristics similar to 55 s period energy, though not as smooth as the latter. Namely, the \vec{A} coefficients are generally orthogonal to the \vec{B} coefficients. The Laplacian of logarithmic amplitudes ($\nabla \cdot \vec{A}$) show trends roughly parallel to the direction of energy propagation, and peak

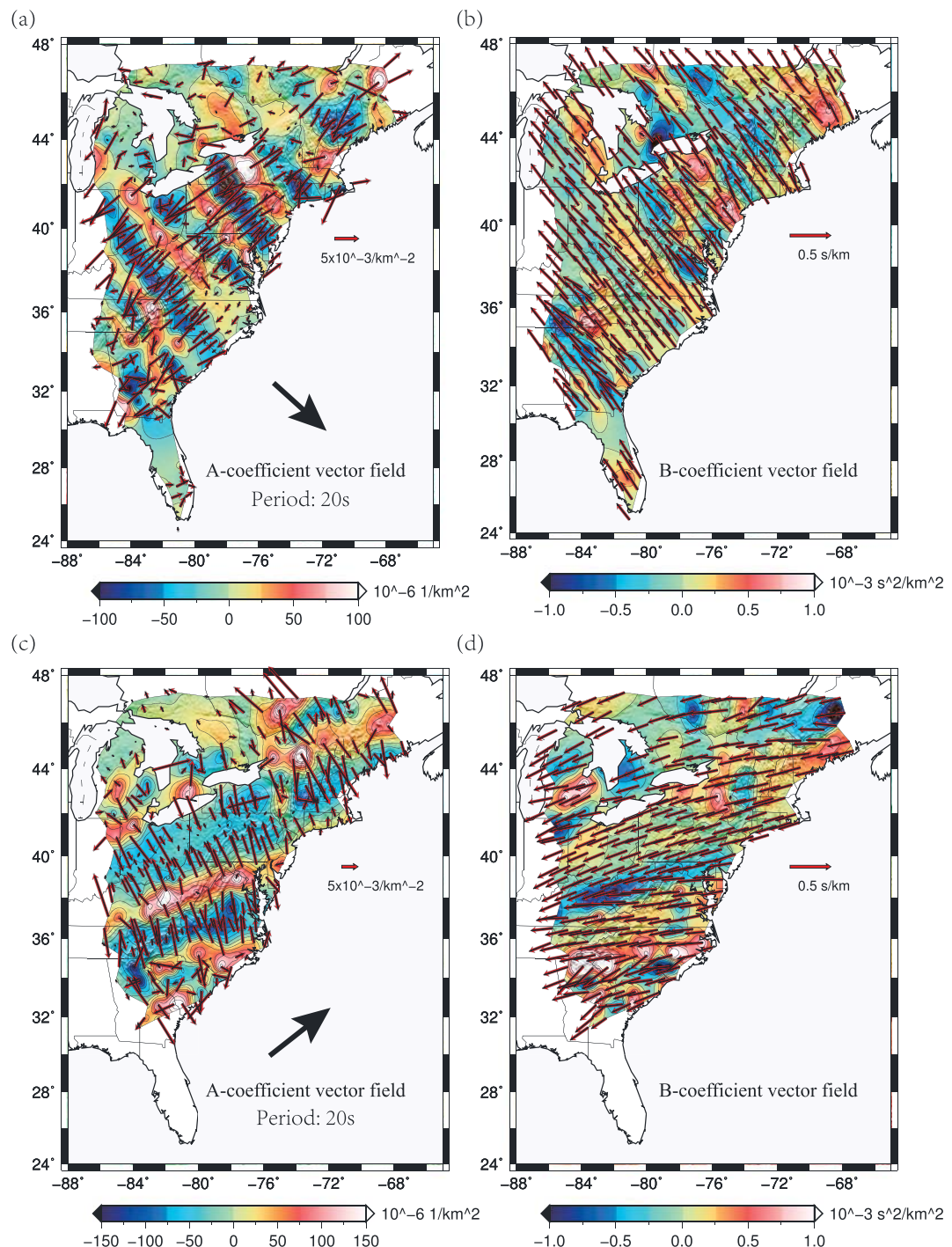


Figure 13. (a and c) Vector fields are associated with \vec{A} coefficients and contours show $\nabla \cdot \vec{A}$ for 20 s Rayleigh wave from 25 October 2013, earthquake near Honshu and 2 February 2014, earthquake near Kermadec Island, respectively. (b and d) Vector fields are associated with \vec{B} coefficients and contours show $\nabla \cdot \vec{B}$ for the same events in Figures 13a and 13b.

values of the Laplacian correspond to amplitude minima and maxima (Figures 13a and 13c). Peak values of Laplacian of logarithmic amplitude also show regions where major focusing and defocusing of energy occurs (coincident with deflections of \vec{B} coefficient in Figures 13b and 13d). These spatial variations in peak-to-peak amplitude are apparently captured by USAArray TA stations spacing (70 km) for 20 s energy. The reason for this is that the length scales of peak-to-peak amplitude variations (measured orthogonal to propagation direction) are generally captured by more than four TA stations. The systematic deflection of \vec{B} coefficient is constrained

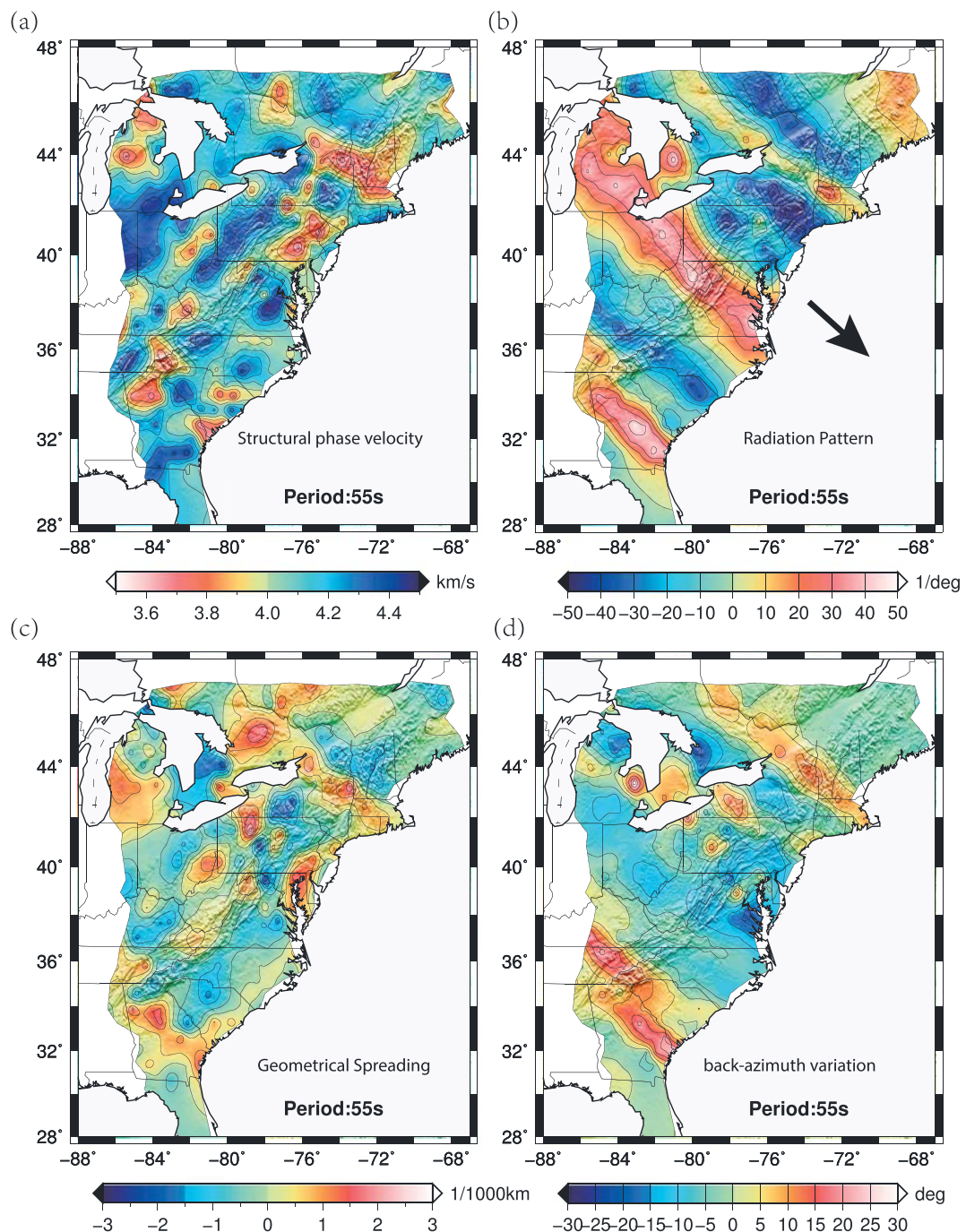


Figure 14. Wave propagation parameters for 55 s Rayleigh wave, estimated from the 25 October 2013, earthquake near Honshu.

over distances of only one station spacing along a trend line connecting central New Jersey to eastern Kentucky (Figure 13d), and this deflection is consistent with a closely adjacent ridge along the same trend where there are major amplitude lows.

Similar to Liang and Langston [2009], we show four wave propagation parameters: phase velocity, radiation pattern, geometrical spreading, and back azimuth variation for the same events. These events show a range of source azimuths but represent typical behaviors observed for most events. We have advanced the gradiometry method to explore approximate solutions to the Helmholtz equation, which provide estimates of the structural phase velocity. Estimates of structural phase velocities differ substantially for some regions,

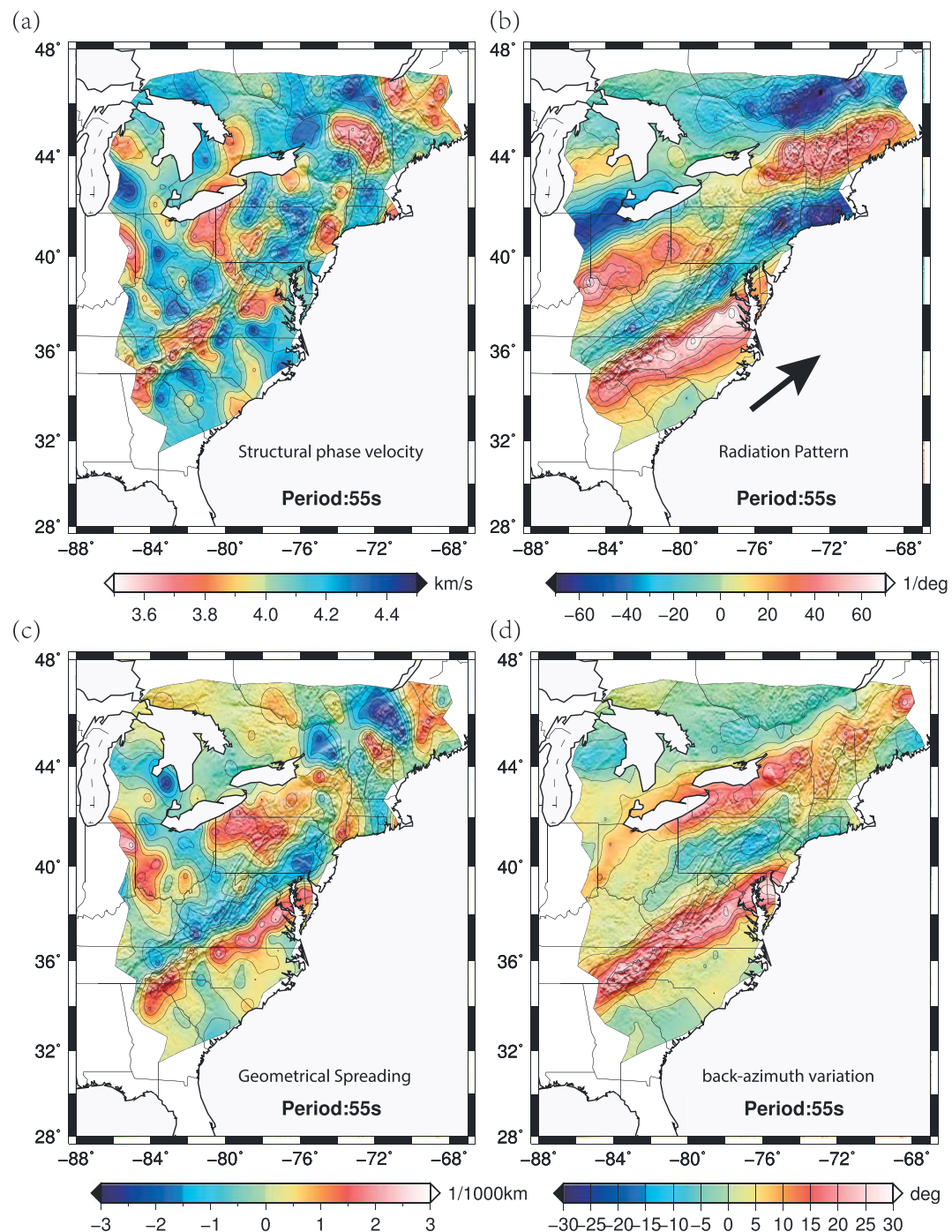


Figure 15. Wave propagation parameters for 55 s Rayleigh wave, estimated from the 2 February 2014, earthquake near Kermadec Island.

obtained from different events (Figures 14a, 15a, 16a, and 17a), which is commonly observed with surface wave analysis [Liang and Langston, 2009; Lin and Ritzwoller, 2011]. The heterogeneous structure along the ray path may introduce strong phase velocity discrepancies for earthquakes coming from different azimuths [Lin and Schmandt, 2014]. However, the azimuthal variation in phase velocities obtained here can provide constraints for azimuthal anisotropy within this region. Furthermore, the presence of anisotropy can produce complexity in the wavefield [Park and Yu, 1993; Yang and Forsyth, 2006; Lin and Schmandt, 2014], and wave gradiometry methods may hold promise for yielding insight into these effects.

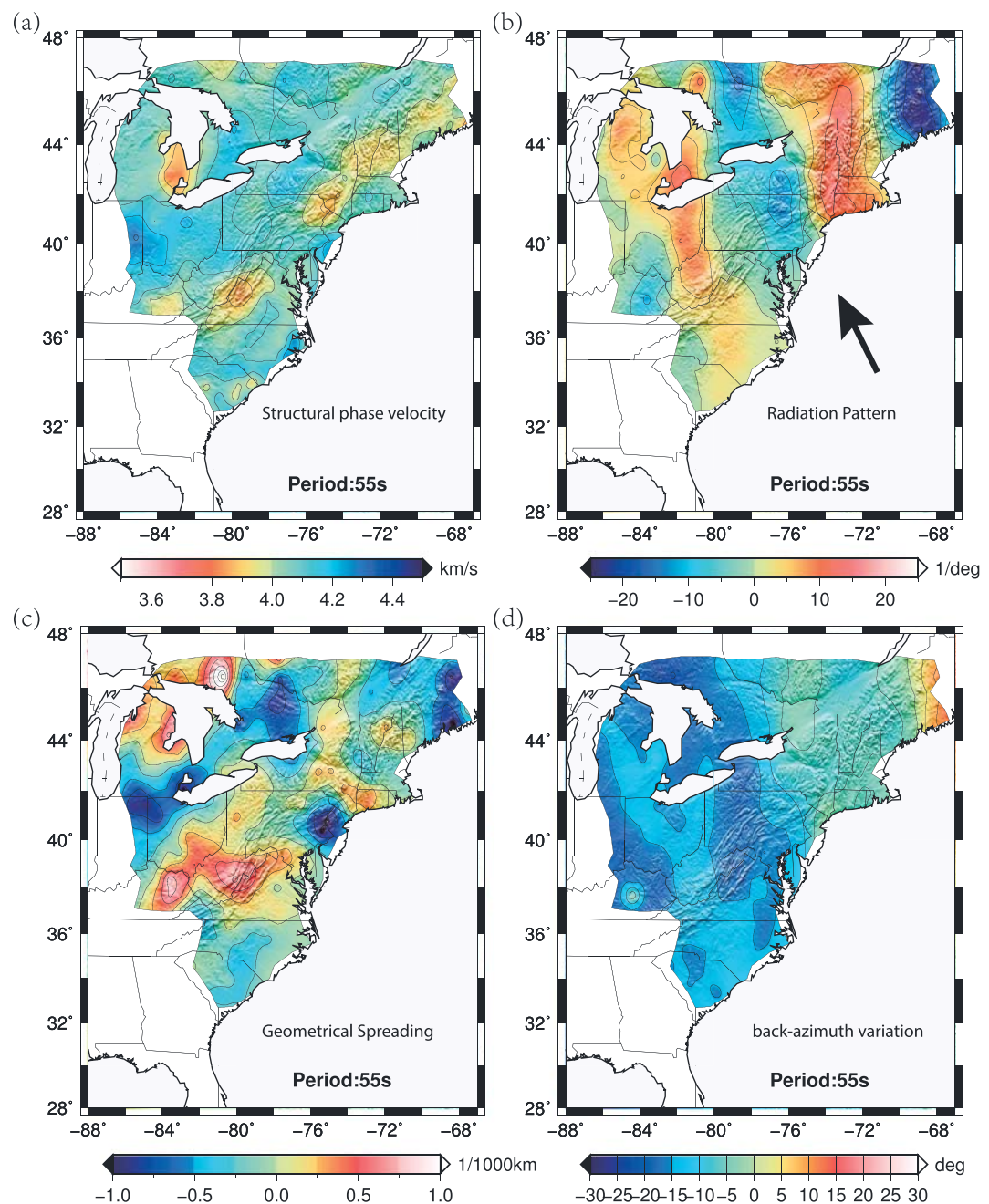


Figure 16. Wave propagation parameters for 55 s Rayleigh wave, estimated from the 16 March 2014, earthquake near Chile.

3.1. 25 October 2013 $M_w = 7.3$ Honshu Event

The Honshu event of 25 October 2013 involves a back azimuth from the northwest. The radiation patterns in Figure 14b show a distribution of ridges that run roughly parallel to the ray path direction. This can be understood by examining Figure 11a, which shows gradients of logarithmic amplitude (\vec{A} coefficients) that are in general orthogonal to propagation direction. Where the \vec{A} coefficient vectors show components that are not orthogonal to the propagation direction, one expects to observe a nonzero value of geometrical spreading, and by transport equation (24) we expect to see nonzero values for $\nabla \cdot \vec{B}$ for these regions. Indeed, we observe a very close positive correlation between the geometrical spreading in Figure 14c and $\nabla \cdot \vec{B}$ in Figure 12a. Positive values of $\nabla \cdot \vec{B}$ highlight regions where the vectors show some divergence, corresponding to curvature of the wavefront. However, because the \vec{B} coefficients point opposite to the direction of wave propagation, positive

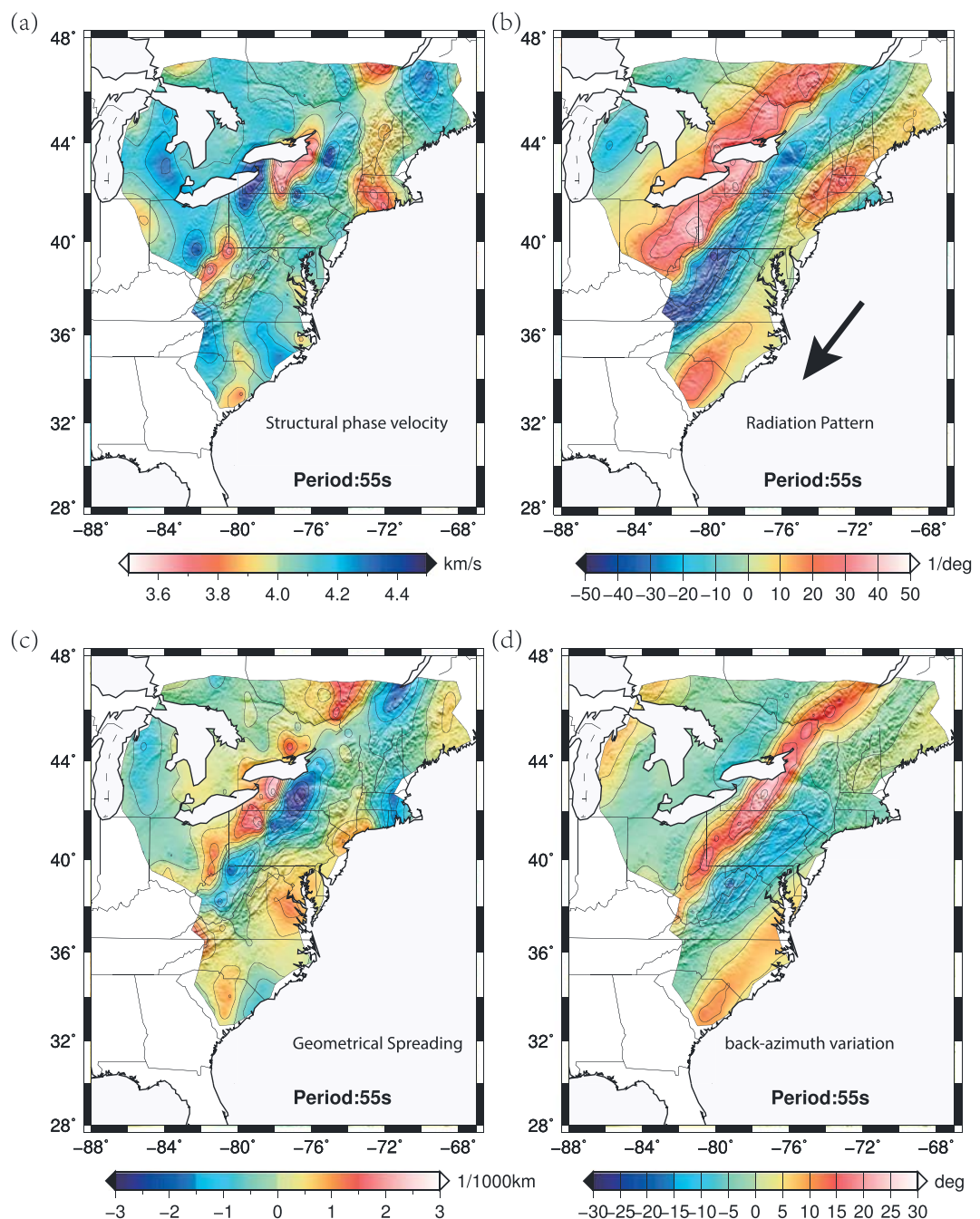


Figure 17. Wave propagation parameters for 55 s Rayleigh wave, estimated from the 24 May 2014, earthquake in Aegean Sea.

values for $\nabla \cdot \vec{B}$ represent regions where the energy is converging or focusing and negative values represent regions where the energy is defocusing (Figure 12a). It is known that heterogeneous structure results in off great circle arrivals [Evernden, 1954]. The back azimuth variation (-30° to 30°) in Figure 14d can be compared with \vec{B} coefficient vectors in Figure 12a to show whether energy is arriving clockwise or anticlockwise to the expected great circle path [Liang and Langston, 2009; Foster et al., 2013]. In general, the geometrical spreading (Figure 14c) and $\nabla \cdot \vec{B}$ (Figure 12a) are both anticorrelated with the Laplacian of logarithmic amplitude (Figure 11a) for most regions. Within regions of energy focusing (i.e., the positive northwest trending band in the U.S. Northeast and Canada (Figures 12a and 14c), we observe negative values for Laplacian of logarithmic

amplitude (Figure 11a), which corresponds to areas of amplitude highs. Within regions of energy defocusing, we generally observe positive values for Laplacian of logarithmic amplitude.

3.2. 2 February 2014 $M_w=6.6$ Kermadec Island Event

The event of 2 February 2014 from Kermadec Island has a back azimuth from the southwest. The Laplacian of logarithmic amplitude (Figure 12b) and the radiation pattern (Figure 15b) both show strong banding with trends that are primarily parallel to propagation direction, which suggests that amplitude variations are dominantly orthogonal to propagation direction. The geometrical spreading (Figure 15c) again shows a strong correlation with $\nabla \cdot \vec{B}$ (Figure 12b), and they are both anticorrelated with the Laplacian of logarithmic amplitude (Figure 11b). For example, there is a strong positive band of Laplacian of logarithmic amplitude extending from eastern Tennessee, trending northeast up into Maryland and southern New Jersey. Examination of Figures 12b and 15c shows that there is a strong defocusing of energy (negative values for geometrical spreading (Figure 15c) and $\nabla \cdot \vec{B}$ (Figure 12b) along this band). Note that path directions are also directed clockwise (Figure 15d)) of expected great circle directions along this band. This deflection of energy clockwise, the negative values for geometrical spreading and $\nabla \cdot \vec{B}$, the positive values for Laplacian of logarithmic amplitude, and the amplitude lows are all consistent with defocusing along this trend.

3.3. 16 March 2014 $M_w = 7.0$ Chile Event

The 16 March 2014 Chile earthquake has a back azimuth from the southeast and again shows similar banding patterns for Laplacian of logarithmic amplitude (Figure 11c) and the radiation pattern (Figure 16b) that suggest strong gradients in amplitude orthogonal to propagation direction. In north and northwest of New Jersey regions, $\nabla \cdot \vec{B}$ is extremely low (Figure 12c), where the geometrical spreading is negative (Figure 16c) and the Laplacian of logarithmic amplitude is strongly positive (Figure 11c), which suggests a strong defocusing of energy.

3.4. 24 May 2014 $M_w = 6.9$ Aegean Sea Event

The event of 24 May 2014 in Aegean Sea shows a back azimuth of energy from the northeast. This event may present the most compelling correlation of geometrical spreading (Figure 17c) with $\nabla \cdot \vec{B}$ (Figure 12d), covering the region from West Virginia to northern New York. Negative values for $\nabla \cdot \vec{B}$ indicates a strong defocusing of energy along this belt, where there are strong positive values for Laplacian of logarithmic amplitude in Figure 11d or amplitude minima.

3.5. Summary From Gradiometry Analysis of Individual Events

In summary, gradiometry parameters provide a rich field of information for each event. A consistent pattern observed to date involves amplitude variations that are primarily in directions orthogonal to wavefield propagation direction. The remarkable correlation between geometrical spreading and $\nabla \cdot \vec{B}$, predicted by transport equation (24), suggests a self-consistent link between the \vec{A} and \vec{B} coefficients that yield information on characteristics of the wavefield, such as where focusing and defocusing of energy is occurring and how it is linked with azimuth of arriving energy and amplitude variations. The apparent satisfaction of equation (24) provided by these several examples of observed wavefields suggests that these measured Rayleigh wave parameters are generally in accord with the second compatibility relation in the Helmholtz equation (see also Figure 4). The positive correlation between $\nabla \cdot \vec{B}$ and geometrical spreading also suggests that $\nabla \cdot \vec{B}$ may be robust enough to use in future work to provide constraints for density variations [Lin *et al.*, 2012].

4. Isotropic Phase Velocity Results

Surface wave azimuthal anisotropy has been observed in the crust [Lin and Schmandt, 2014] and upper mantle [Beghein *et al.*, 2010; Lin and Ritzwoller, 2011] across the United States. We expect that the stacking of results from multiple events is able to reduce the effect of azimuthal anisotropy [Liang and Langston, 2009; Foster *et al.*, 2013]. The isotropic phase velocity results for 12 period bands are shown in Figures 18–20. The phase velocity generally increases with period from 3.5 km/s to 4.5 km/s and is consistent with the theoretical dispersion curve [Dahlen and Tromp, 1998]. The formal standard error of phase velocity for any given event is less than 1%. However, the dispersion of data from multiple azimuths yields a variation in phase velocity with standard errors of around 3%. The dynamic and structural phase velocity differences decrease from 0.4 km/s for individual events to 0.1–0.2 km/s for isotropic results. However, we do observe that these differences increase with period, especially for periods longer than 50 s, which may account for finite frequency effects. Lin and Ritzwoller [2011] also draw similar conclusions from observations in the western U.S.

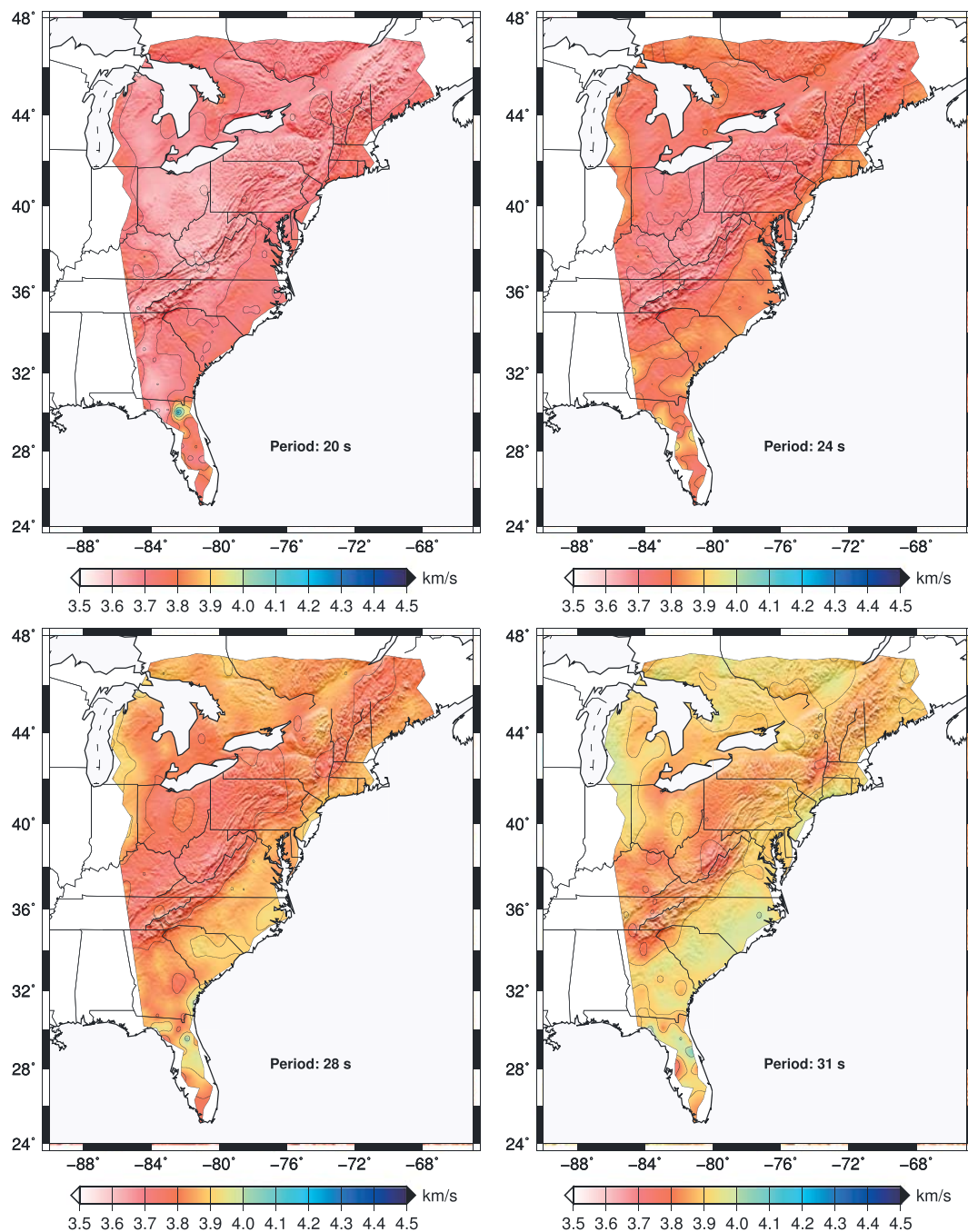


Figure 18. Isotropic phase velocities for 20 s–31 s Rayleigh wave. Contours are separated by intervals of 0.1 km/s.

Results for 20 s, 24 s, 28 s, and 31 s periods show a clear transition from higher to lower velocity along the easternmost boundary of the Appalachian topography, corresponding approximately to the location of the early Paleozoic continental margin boundary [Cook and Oliver, 1981]. We also observe two distinct low-velocity zone anomalies for 37 s, 40 s, 44 s, and 49 s periods: one centered along the Virginia-West Virginia state boundary and the other one located in Vermont, New Hampshire and easternmost New York. The anomalies persist within both regions for longer periods out to 112 s, but they are weaker for these longer periods. The anomaly in Virginia/west Virginia border region may be associated, in part, with the thicker crust beneath the Appalachians [Parker *et al.*, 2013], but the presence for the longer periods may suggest a persistence of this anomaly within the upper mantle. These low-velocity zones are consistent with surface wave tomography results from Jin and Gaherty [2015], and *P* and *S* wave velocity models at depths of

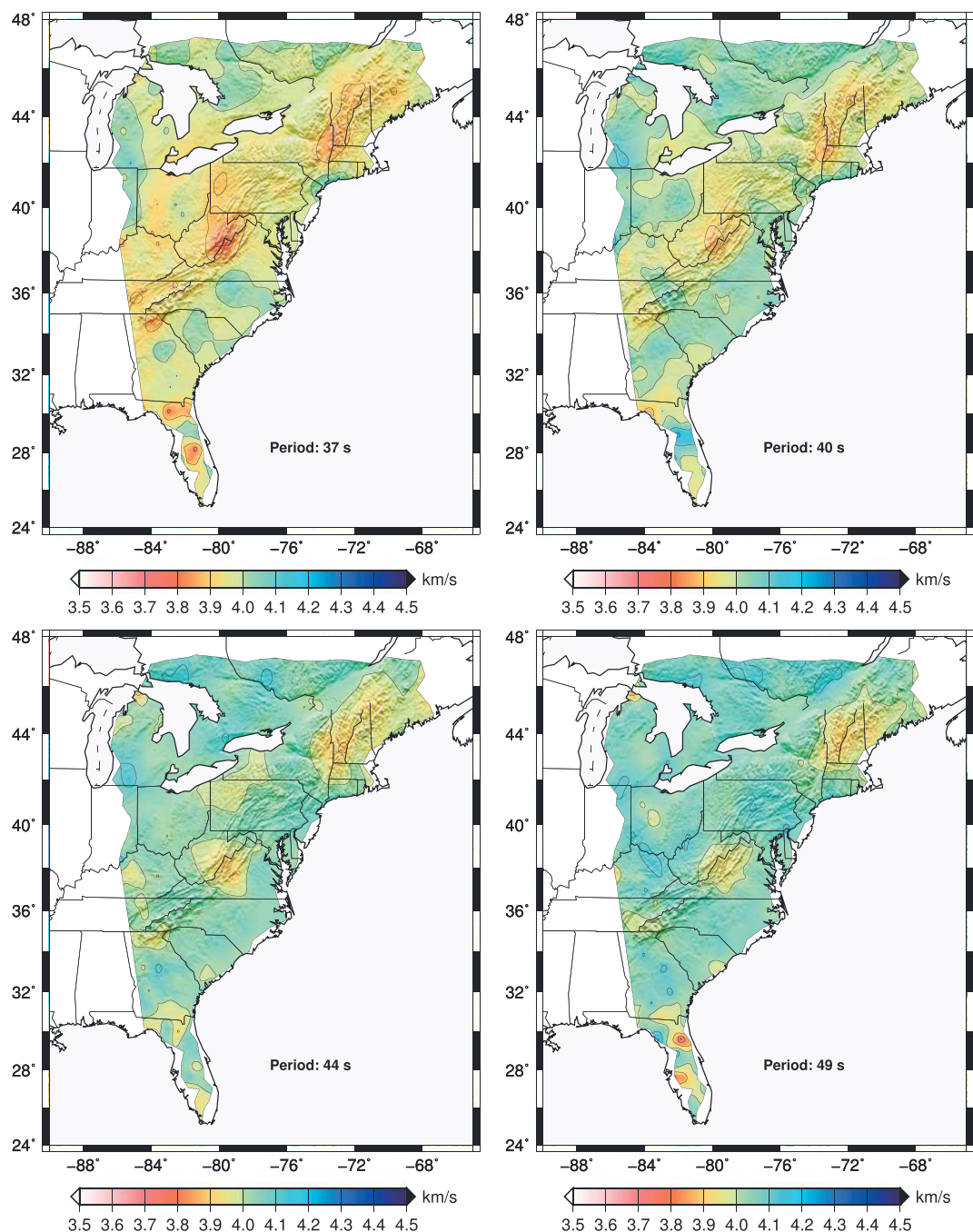


Figure 19. Isotropic phase velocities for 37 s–49 s Rayleigh wave. Contours are separated by intervals of 0.1 km/s.

60–300 km obtained by Schmandt and Lin [2014]. Liang and Langston [2008] observed the 15 s Rayleigh wave low group velocity anomalies around the center part of the Appalachian Mountains. A 3-D S velocity model of upper mantle beneath U.S., NA04, [van der Lee and Frederiksen, 2005] also revealed the northern anomaly feature even prior to the arrival of USArray to the northeastern U.S. Eaton and Frederiksen [2007] and Villemaire *et al.* [2012] claim this anomaly coincides with the inferred track of Great Meteor hotspot, which extends from northern Hudson bay to the northeast U.S. coast, and continues southeast as a chain of seamounts in the Atlantic ocean [Duncan, 1984]. Schmandt and Lin [2014] pointed out that the passive margin region has experienced Eocene basaltic volcanism at 48 Ma [Mazza *et al.*, 2014], and the center of the low-velocity anomaly we observe beneath the border of Virginia-West Virginia corresponds to the location of this

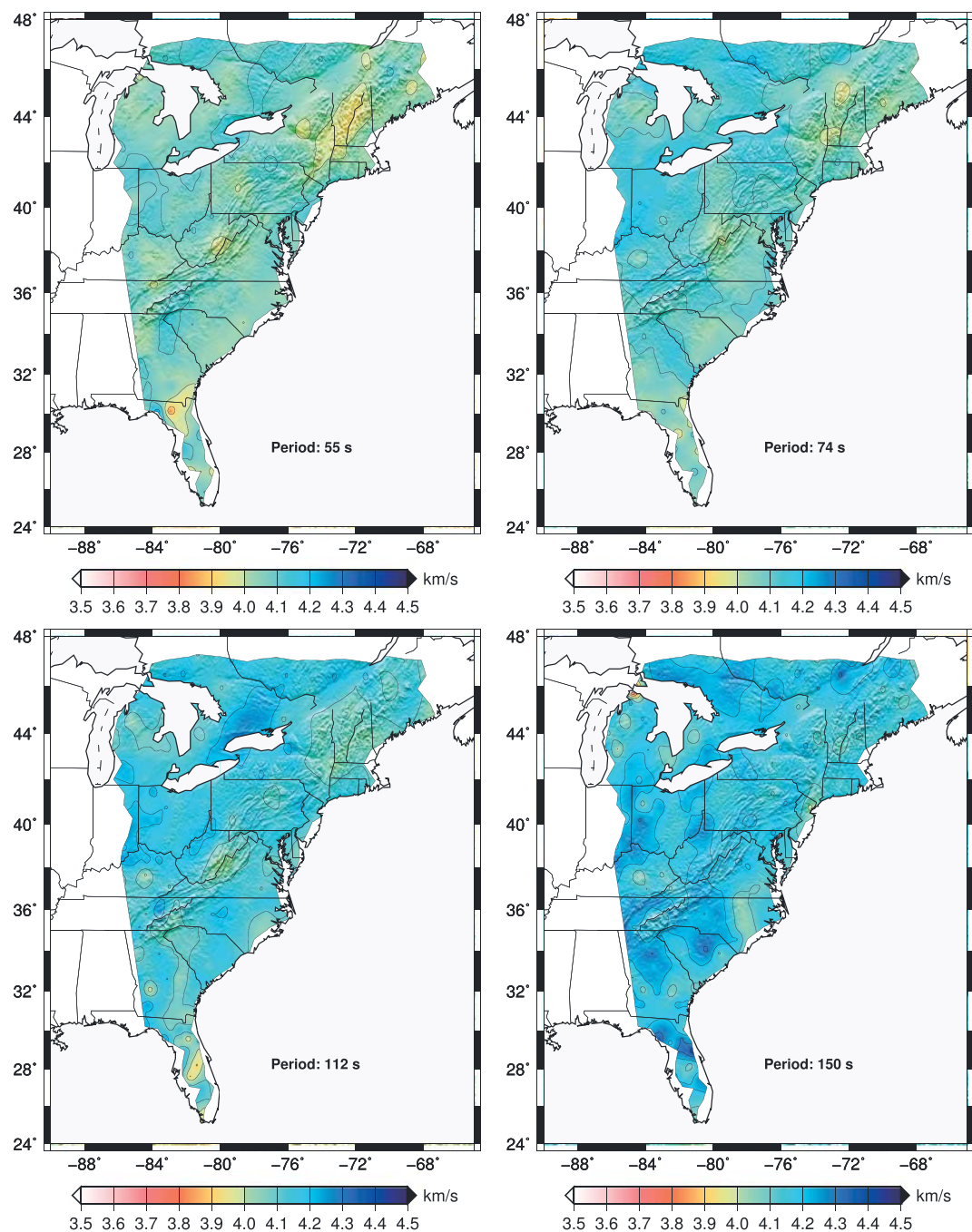


Figure 20. Isotropic phase velocities for 55 s–150 s Rayleigh wave. Contours are separated by intervals of 0.1 km/s.

volcanism. We discard several bad stations located around southern Alabama and Northern Kentucky, which are the least-well resolved regions due to edge effects.

5. Discussion and Conclusions

We use a modified wave gradiometry method to process 37 events recorded by around 450 USArray TA stations in the eastern U.S. Compared to traditional ray-based tomographic techniques, the advantage of wave gradiometry is that the spatial variations of wave amplitudes across the whole array are taken into account, which further provides an approximate solution to the Helmholtz equation. Consequently, the effects from local geometry of the wavefield and phase interferences are greatly decreased [Wielandt, 1993].

The gradiometry results for any given event provide insight into the link between variations in geometrical spreading, back azimuth variations, focusing and defocusing of energy, radiation patterns, and amplitude variations.

In the wave gradiometry method we first obtain the displacements and the time derivatives of displacement field. We then calculate the spatial gradients of displacement field through bicubic spline interpolation, for the shifted waveforms within a subarray. We then solve for the \vec{A} and \vec{B} coefficients iteratively, using damped least squares inversion with smoothing, which enables us to estimate phase velocity, changes in geometrical spreading, radiation pattern, and back azimuth variations. It turns out that the \vec{A} coefficient corresponds to the gradient of logarithmic amplitude, and the inverse of \vec{B} coefficient provides an approximation to the dynamic phase velocity. Thus, we interpolate \vec{A} and \vec{B} coefficient vectors using the same bicubic spline method, to obtain $\nabla \cdot \vec{A}$, corresponding to the Laplacian of logarithmic amplitude, and $\nabla \cdot \vec{B}$, corresponding to an approximation to the Laplacian of phase travelttime. The \vec{A} coefficients, along with $\nabla \cdot \vec{A}$, enable us to calculate the amplitude correction term for structural phase velocity.

Finally, we stack Rayleigh wave structural phase velocity results from 37 earthquakes for 15 passbands with center periods ranging from 20 s to 150 s to get isotropic phase velocity maps, which show an interesting contrast between the Piedmont and Coastal Plain regions and the interior Appalachian chain. This velocity contrast is observed close to the boundary of the early Paleozoic continental margin location [Cook and Oliver, 1981] and is present for periods 20 s–31 s. We also observe two prominent low-velocity zones for periods 37 s–49 s: one in the central Appalachians, centered along the Virginia–West Virginia border region and the other in the northeast located in Vermont, New Hampshire and easternmost New York. The anomalies persist for the longer periods out to 112 s but are not as strong. The central Appalachian anomaly is located in the region of Eocene basaltic volcanism [Mazza et al., 2014; Schmandt and Lin, 2014], and the northeast low-velocity anomaly is thought to correspond to the meteor hotspot track [Eaton and Frederiksen, 2007; Villemaire et al., 2012].

In general, geometrical spreading and $\nabla \cdot \vec{B}$ are strongly correlated, but these two are anticorrelated with Laplacian of logarithmic amplitude or $\nabla \cdot \vec{A}$. The angle difference between the energy propagation direction and the expected great circle path can be as large as $\pm 30^\circ$ (back azimuth variations). The links between radiation pattern, geometrical spreading, and structural phase velocity represents areas of energy focusing/defocusing that still require exploration. We find that the gradiometry parameter distributions are unique for any given event and associated ray path. A complete structural interpretation for the diverse distributions of gradiometry parameters obtained from 37 events, with 15 period bands for each event, is beyond the scope of this paper. However, one future application, involving solutions to the wave equation for full 3-D structure [Tape et al., 2009; Zhu et al., 2015], may be to model such spatial variations in radiation, geometrical spreading, back azimuth, and structural phase velocity for any given event. That is, a match between synthetic and observed gradiometry parameters has the potential to rigorously ensure a viable structural interpretation by providing a broader set of wavefield observables. The azimuthal anisotropy can also be explored by studying the phase velocity maps obtained from individual earthquakes. Moreover, \vec{A} , \vec{B} , $\nabla \cdot \vec{A}$, and $\nabla \cdot \vec{B}$ can be used to infer density information along the ray path.

We have investigated two separate compatibility relations: one in the wave equation solution (1) and the other in the Helmholtz equation solution (17) and have shown that each relation can provide useful information on the characteristics of the wavefield. The assumptions embedded in equation (1) involve a single dominant phase [Langston, 2007a], and the slowness for this phase can be recovered using the gradiometry method. The Helmholtz equation results in an amplitude correction term that can be substantial if the amplitude variations are large. The question arises as to the link between the slowness embedded in the gradiometry \vec{B} coefficient and the structural phase velocity arising from the Helmholtz treatment. The slowness defined in equation (7) is not necessarily equal to the gradient of phase travelttime embedded in equation (17), unless this gradient precisely defines the local ray slowness for a single phase. In general, this is unlikely to be true due to finite frequency, multipathing, and scattering effects. However, we find that the slowness field obtained using gradiometry assumptions generally provides excellent agreement with results obtained using gradient of phase travelttime methods [Lin and Ritzwoller, 2011]. This empirical result has led us to make the approximation that the \vec{B} coefficient is approximately equal to the gradient of phase travelttime, and thus it is valid to explore the amplitude correction term embedded in Helmholtz treatment. Both Wielandt [1993] and

Lin and Ritzwoller [2011] have shown that there are substantial amplitude correction terms where there is strong wavefront curvature.

It is important to keep in mind that both equations (1) and (17) involve approximations of the real wavefield yet employing both provide important insights into the nature of that wavefield. We have shown that the gradiometry method can provide realistic estimates of the slowness of the local wavefield along with estimates of amplitude correction terms. Our results show a strong link between amplitude variations and the focusing/defocusing of energy (reflected in $\nabla \cdot \vec{B}$) associated with the wavefront curvature, which we are able to resolve over length scales about twice the station spacing. We argue that in the presence of wavefront curvature it is valid to investigate the second compatibility relation in the Helmholtz equation in order to explore the effects of the amplitude correction terms. These corrections may be justified due to the strong local curvature of the wavefront [*Friederich et al.*, 1995]. We find that only where there is strong curvature of the wavefront are there significant amplitude correction terms, providing significant differences between dynamic and structural phase velocity. In regions where wave gradiometry shows no curvature, we find little to no amplitude correction and dynamic phase velocity equals structural phase velocity. One great value of gradiometry, therefore, is to show where the wavefield has complexity. Further work is needed to better understand the link between gradiometry parameters obtained from assumptions in equation (1), the amplitude correction terms associated with the separate Helmholtz treatment in equation (17), and the effects of true structural complexity on the inferred results. Again, the investigation with full 3-D synthetics associated with structural complexity will be necessary to fully explore this link.

Acknowledgments

The authors would like to thank Charles Langston and another anonymous reviewer for their helpful comments to improve the manuscript. Data from the TA network used in this study were made freely available as part of the EarthScope USArray facility, operated by Incorporated Research Institutions for Seismology (IRIS), and supported by the National Science Foundation, under Cooperative Agreements EAR-1261681. This work used the supercomputing facility: Extreme Science and Engineering Discovery Environment (XSEDE), which is supported by National Science Foundation grant ACI-1053575. This research was supported by National Science Foundation grants EAR-1052989, EAR-1246971, EAR-1358613, and EAR-140001.

References

- Aster, R. C., B. Borchers, and C. H. Thurber (2011), *Parameter Estimation and Inverse Problems*, Elsevier Acad. Press, Waltham, Mass.
- Beavan, J., and J. Haines (2001), Contemporary horizontal velocity and strain rate fields of the Pacific-Australian plate boundary zone through New Zealand, *J. Geophys. Res.*, 106(B1), 741–770, doi:10.1029/2000JB900302.
- Beghein, C., J. A. Snoke, and M. J. Fouch (2010), Depth constraints on azimuthal anisotropy in the great basin from rayleigh-wave phase velocity maps, *Earth Planet. Sci. Lett.*, 289(3), 467–478, doi:10.1016/j.epsl.2009.11.036.
- Birtill, J. W., and F. E. Whiteway (1965), The application of phased arrays to analysis of seismic body waves, *Philos. Trans. R. Soc. London, Ser. A*, 258, 421–493, doi:10.1098/rsta.1965.0048.
- Bodin, T., and V. Maupin (2008), Resolution potential of surface wave phase velocity measurements at small arrays, *Geophys. J. Int.*, 172(2), 698–706, doi:10.1111/j.1365-246X.2007.03668.x.
- Brudzinski, M. R., and R. M. Allen (2007), Segmentation in episodic tremor and slip all along Cascadia, *Geology*, 35(10), 907–910, doi:10.1130/g23740a.1.
- Burdick, S., R. D. van der Hilst, F. L. Vernon, V. Martynov, T. Cox, J. Eakins, G. H. Karas, J. Tylell, L. Astiz, and G. L. Pavlis (2014), Model update January 2013: Upper mantle heterogeneity beneath North America from travel-time tomography with global and USArray transportable array data, *Seismol. Res. Lett.*, 85(1), 77–81, doi:10.1785/0220130098.
- Cao, A., and A. Levander (2010), High-resolution transition zone structures of the gorda slab beneath the western United States: Implication for deep water subduction, *J. Geophys. Res.*, 115, B07301, doi:10.1029/2009JB006876.
- Cerveny, V. (2005), *Seismic Ray Theory*, Cambridge Univ. Press, Cambridge, U.K.
- Cook, F. A., and J. E. Oliver (1981), The late Precambrian-early Paleozoic continental edge in the Appalachian orogen, *Am. J. Sci.*, 281(8), 993–1008.
- Dahlen, F. A., and J. Tromp (1998), *Theoretical Global Seismology*, Princeton Univ. Press, Princeton, N. J.
- De Boor, C. (1987), *A Practical Guide to Splines*, 392 pp., Springer, New York.
- Duncan, R. A. (1984), Age progressive volcanism in the New England seamounts and the opening of the central Atlantic Ocean, *J. Geophys. Res.*, 89(B12), 9980–9990, doi:10.1029/JB089B12p09980.
- Eaton, D. W., and A. Frederiksen (2007), Seismic evidence for convection-driven motion of the North American plate, *Nature*, 446(7134), 428–431, doi:10.1038/nature05675.
- Evanzia, D., J. Pulliam, R. Ainsworth, H. Gurrola, and K. Pratt (2014), Seismic Vp and Vs tomography of Texas and Oklahoma with a focus on the Gulf Coast margin, *Earth Planet. Sci. Lett.*, 402, 148–156, doi:10.1016/j.epsl.2013.12.027.
- Evernden, J. F. (1954), Direction of approach of rayleigh waves and related problems (part II), *Bull. Seismol. Soc. Am.*, 44(2A), 159–184.
- Foster, A., G. Ekström, and M. Nettles (2013), Surface wave phase velocities of the western United States from a two-station method, *Geophys. J. Int.*, 196, 1189–1206, doi:10.1093/gji/ggt454.
- Friederich, W., E. Wielandt, and S. Stange (1995), Non-plane geometries of seismic surface wavefields and their implications for regional surface-wave tomography, *Geophys. J. Int.*, 119, 931–948, doi:10.1111/j.1365-246X.1994.tb04026.x.
- Friederich, W., S. Hunzinger, and E. Wielandt (2000), A note on the interpretation of seismic surface waves over 3-D structures, *Geophys. J. Int.*, 143, 335–339.
- Ghosh, A., and E. W. Holt (2012), Plate motions and stresses from global dynamic models, *Science*, 335(6070), 838–43, doi:10.1126/science.1214209.
- Ghosh, A., W. E. Holt, and L. Wen (2013), Predicting the lithospheric stress field and plate motions by joint modeling of lithosphere and mantle dynamics, *J. Geophys. Res. Solid Earth*, 118, 346–368, doi:10.1029/2012JB009516.
- Haines, A. J., and E. W. Holt (1993), A procedure for obtaining the complete horizontal motions within zones of distributed deformation from the inversion of strain rate data, *J. Geophys. Res.*, 98(B7), 12,057–12,082, doi:10.1029/93JB00892.
- Holt, E. W., and G. Shcherbenko (2013), Toward a continuous monitoring of the horizontal displacement gradient tensor field in southern California using GPS observations from Plate Boundary Observatory (PBO), *Seismol. Res. Lett.*, 84(3), 455–467, doi:10.1785/0220130004.
- Holt, E. W., N. Chamot-Rooke, X. Le Pichon, A. J. Haines, B. Shen-Tu, and J. Ren (2000a), Velocity field in Asia inferred from quaternary fault slip rates and global positioning system observations, *J. Geophys. Res.*, 105(B8), 19,185–19,209, doi:10.1029/2000JB900045.

- Holt, E. W., B. Shen-Tu, A. J. Haines, and J. Jackson (2000b), On the determination of self-consistent strain rate fields within zones of distributed continental deformation, in *History and Dynamics of Global Plate Motions*, edited by M. A. Richards, R. G. Gordon, and R. D. Van Der Hilst, AGU, Washington, D. C., doi:10.1029/GM121p0113.
- Jin, G., and J. B. Gaherty (2015), Surface wave phase-velocity tomography based on multichannel cross-correlation, *Geophys. J. Int.*, 201(3), 1383–1398, doi:10.1093/gji/ggv079.
- Knopoff, L., S. Mueller, and W. L. Pilant (1966), Structure of the crust and upper mantle in the Alps from the phase velocity of Rayleigh waves, *Bull. Seismol. Soc. Am.*, 56(5), 1009–1044.
- Langston, C. A. (2006), Explosion source strong ground motions in the Mississippi Embayment, *Bull. Seismol. Soc. Am.*, 96(3), 1038–1054, doi:10.1785/0120050105.
- Langston, C. A. (2007a), Spatial gradient analysis for linear seismic arrays, *Bull. Seismol. Soc. Am.*, 97(1B), 265–280, doi:10.1785/0120060100.
- Langston, C. A. (2007b), Wave gradiometry in two dimensions, *Bull. Seismol. Soc. Am.*, 97(2), 401–416, doi:10.1785/0120060138.
- Langston, C. A. (2007c), Wave gradiometry in the time domain, *Bull. Seismol. Soc. Am.*, 97(3), 926–933, doi:10.1785/0120060152.
- Langston, C. A., and S. P. Horton (2014), Three-dimensional seismic-velocity model for the unconsolidated Mississippi Embayment sediments from H/V ambient noise measurements, *Bull. Seismol. Soc. Am.*, 104(5), 2349–2358, doi:10.1785/0120140026.
- Levander, A., B. Schmandt, M. S. Miller, K. Liu, K. E. Karlstrom, R. S. Crow, C. T. Lee, and E. D. Humphreys (2011), Continuing Colorado plateau uplift by delamination-style convective lithospheric downwelling, *Nature*, 472(7344), 461–465, doi:10.1038/nature10001.
- Liang, C., and C. A. Langston (2008), Ambient seismic noise tomography and structure of eastern North America, *J. Geophys. Res.*, 113, B03309, doi:10.1029/2007JB005350.
- Liang, C., and C. A. Langston (2009), Wave gradiometry for USArray: Rayleigh waves, *J. Geophys. Res.*, 114, B02308, doi:10.1029/2008JB005918.
- Lin, F.-C., and M. H. Ritzwoller (2011), Helmholtz surface wave tomography for isotropic and azimuthally anisotropic structure, *Geophys. J. Int.*, 186(3), 1104–1120, doi:10.1111/j.1365-246X.2011.05070.x.
- Lin, F.-C., and B. Schmandt (2014), Upper crustal azimuthal anisotropy across the contiguous U.S. determined by Rayleigh wave ellipticity, *Geophys. Res. Lett.*, 41, 8301–8307, doi:10.1002/2014GL062362.
- Lin, F.-C., M. P. Moschetti, and M. H. Ritzwoller (2008), Surface wave tomography of the western United States from ambient seismic noise: Rayleigh and Love wave phase velocity maps, *Geophys. J. Int.*, 173(1), 281–298, doi:10.1111/j.1365-246X.2008.03720.x.
- Lin, F.-C., M. H. Ritzwoller, and R. Snieder (2009), Eikonal tomography: Surface wave tomography by phase front tracking across a regional broad-band seismic array, *Geophys. J. Int.*, 177(3), 1091–1110, doi:10.1111/j.1365-246X.2009.04105.x.
- Lin, F.-C., V. C. Tsai, and M. H. Ritzwoller (2012), The local amplification of surface waves: A new observable to constrain elastic velocities, density, and anelastic attenuation, *J. Geophys. Res.*, 117, B06302, doi:10.1029/2012JB009208.
- Lin, F.-C., V. C. Tsai, and B. Schmandt (2014), 3-D crustal structure of the western United States: Application of Rayleigh-wave ellipticity extracted from noise cross-correlations, *Geophys. J. Int.*, 198(2), 656–670, doi:10.1093/gji/ggu160.
- Mazza, S. E., E. A. Johnson, M. J. Kunk, R. McAleer, J. A. Spotila, M. Bizimis, and D. S. Coleman (2014), Volcanoes of the passive margin: The youngest magmatic event in eastern North America, *Geology*, 42(6), 483–486, doi:10.1130/G35407.1.
- Meier, T., K. Dietrich, B. Stöckhert, and H. P. Harjes (2004), One-dimensional models of shear wave velocity for the eastern Mediterranean obtained from the inversion of Rayleigh wave phase velocities and tectonic implications, *Geophys. J. Int.*, 156(1), 45–58, doi:10.1111/j.1365-246X.2004.02121.x.
- Obrebski, M., R. M. Allen, F. Pollitz, and S. -H. Hung (2011), Lithosphere-asthenosphere interaction beneath the western United States from the joint inversion of body-wave traveltimes and surface-wave phase velocities, *Geophys. J. Int.*, 185(2), 1003–1021, doi:10.1111/j.1365-246X.2011.04990.x.
- Park, J., and Y. Yu (1993), Seismic determination of elastic anisotropy and mantle flow, *Science*, 261, 1159–1159.
- Parker, E. H., R. B. Hawman, K. M. Fischer, and L. S. Wagner (2013), Crustal evolution across the southern Appalachians: Initial results from the sesame broadband array, *Geophys. Res. Lett.*, 40, 3853–3857, doi:10.1002/grl.50761.
- Pollitz, F. F., and W. D. Mooney (2014), Seismic structure of the central US crust and shallow upper mantle: Uniqueness of the reelfoot rift, *Earth Planet. Sci. Lett.*, 402, 157–166, doi:10.1016/j.epsl.2013.05.042.
- Pollitz, F. F., and J. A. Snook (2010), Rayleigh-wave phase-velocity maps and three-dimensional shear velocity structure of the western US from local non-plane surface wave tomography, *Geophys. J. Int.*, 180(3), 1153–1169, doi:10.1111/j.1365-246X.2009.04441.x.
- Porritt, R. W., R. M. Allen, and F. F. Pollitz (2014), Seismic imaging east of the Rocky Mountains with USArray, *Earth Planet. Sci. Lett.*, 402, 16–25, doi:10.1016/j.epsl.2013.10.034.
- Schmandt, B., and E. Humphreys (2010), Complex subduction and small-scale convection revealed by body-wave tomography of the western United States upper mantle, *Earth Planet. Sci. Lett.*, 297(3–4), 435–445, doi:10.1016/j.epsl.2010.06.047.
- Schmandt, B., and E. Humphreys (2011), Seismically imaged relict slab from the 55 Ma Siletzia accretion to the northwest United States, *Geology*, 39(2), 175–178, doi:10.1130/g31558.1.
- Schmandt, B., and F.-C. Lin (2014), P and S wave tomography of the mantle beneath the United States, *Geophys. Res. Lett.*, 41, 6342–6349, doi:10.1002/2014GL061231.
- Shen, W., M. H. Ritzwoller, and V. Schulte-Pelkum (2013a), A 3-D model of the crust and uppermost mantle beneath the central and western US by joint inversion of receiver functions and surface wave dispersion, *J. Geophys. Res. Solid Earth*, 118, 262–276, doi:10.1029/2012JB009602.
- Shen, W., M. H. Ritzwoller, and V. Schulte-Pelkum (2013b), Crustal and uppermost mantle structure in the central U.S. encompassing the mid-continent rift, *J. Geophys. Res. Solid Earth*, 118, 4325–4344, doi:10.1002/jgrb.50321.
- Sigloch, K., N. McQuarrie, and G. Nolet (2008), Two-stage subduction history under North America inferred from multiple-frequency tomography, *Nat. Geosci.*, 1(7), 458–462, doi:10.1038/ngeo231.
- Sun, D., and D. Helmberger (2011), Upper-mantle structures beneath USArray derived from waveform complexity, *Geophys. J. Int.*, 184(1), 416–438, doi:10.1111/j.1365-246X.2010.04847.x.
- Tape, C., Q. Liu, A. Maggi, and J. Tromp (2009), Adjoint tomography of the southern California crust, *Science*, 325(5943), 988–992, doi:10.1126/science.1175298.
- Towns, J., et al. (2014), XSEDE: Accelerating scientific discovery, *Comput. Sci. Eng.*, 16(5), 62–74, doi:10.1109/MCSE.2014.80.
- van der Lee, S., and A. Frederiksen (2005), Surface wave tomography applied to the North American upper mantle, in *Seismic Earth: Array Analysis of Broadband Seismograms*, vol. 157, edited by A. Levander and G. Nolet, pp. 67–80, AGU, Washington, D. C., doi:10.1029/157GM05.
- Villemaire, M., F. A. Derbyshire, and I. D. Bastow (2012), P-wave tomography of eastern North America: Evidence for mantle evolution from Archean to Phanerozoic, and modification during subsequent hot spot tectonism, *J. Geophys. Res.*, 117, B12302, doi:10.1029/2012JB009639.

- West, J. D., M. J. Fouch, J. B. Roth, and L. T. Elkins-Tanton (2009), Vertical mantle flow associated with a lithospheric drip beneath the great basin, *Nat. Geosci.*, 2(6), 439–444, doi:10.1038/ngeo526.
- Whitmeyer, S. (2007), Tectonic model for the Proterozoic growth of North America, *Geosphere*, 3(4), 220–259, doi:10.1130/ges00055.1.
- Wielandt, E. (1993), Propagation and structural interpretation of non-plane waves, *Geophys. J. Int.*, 113, 45–53.
- Williams, L. M., K. M. Fisher, J. T. Freymueller, B. Tikoff, and A. M. Trehearne (2010), Unlocking the secrets of the North American continent: An EarthScope science plan for 2010–2020, 78 pp. [Available at www.earthscope.org/ESSP, accessed October 4, 2010.]
- Yang, Y., and D. W. Forsyth (2006), Rayleigh wave phase velocities, small-scale convection, and azimuthal anisotropy beneath southern California, *J. Geophys. Res.*, 111, B07306, doi:10.1029/2005JB004180.
- Yang, Y., and M. H. Ritzwoller (2008), Teleseismic surface wave tomography in the western U.S. using the transportable array component of USArray, *Geophys. Res. Lett.*, 35, L04308, doi:10.1029/2007GL032278.
- Yuan, H., and B. Romanowicz (2010), Depth dependent azimuthal anisotropy in the western US upper mantle, *Earth Planet. Sci. Lett.*, 300(3–4), 385–394, doi:10.1016/j.epsl.2010.10.020.
- Zhu, H., E. Bozdağ, and J. Tromp (2015), Seismic structure of the European upper mantle based on adjoint tomography, *Geophys. J. Int.*, 201(1), 18–52, doi:10.1093/gji/ggu492.